Physics   Faculty Publications & Research

2001

Kinematics of the Parsec-Scale Relativistic Jet in Quasar 3C 279: 1991-1997

A. E. Wehrle

B. G. Piner
Whittier College, gpiner@whittier.edu

S. C. Unwin

A. C. Zook

W. Xu

See next page for additional authors

Recommended Citation

Authors

A. E. Wehrle, B. G. Piner, S. C. Unwin, A. C. Zook, W. Xu, A. P. Marscher, H. Terasranta, and E. Valtaoja

KINEMATICS OF THE PARSEC-SCALE RELATIVISTIC JET IN QUASAR 3C 279: 1991–1997

A. E. WEHRLE,[1] B. G. PINER,[1,2] S. C. UNWIN,[1] A. C. ZOOK,[3] W. XU,[4] A. P. MARSCHER,[5]
H. TERÄSRANTA,[6] AND E. VALTAOJA[7,8]

ABSTRACT

We present results of long-term high-frequency VLBI monitoring of the relativistic jet in 3C 279, consisting of 18 epochs at 22 GHz from 1991 to 1997 and 10 epochs at 43 GHz from 1995 to 1997. Three major results of this study are apparent speeds measured for six superluminal components range from $4.8c$ to $7.5c$ ($H_0 = 70$ km s^{-1} Mpc^{-1}, $q_0 = 0.1$), variations in the total radio flux are due primarily to changes in the VLBI core flux, and the uniform-sphere brightness temperature of the VLBI core is $\sim 1 \times 10^{13}$ K at 22 GHz after 1995, one of the highest direct estimates of a brightness temperature. If the variability brightness temperature measured for 3C 279 by Lähteenmäki & Valtaoja is an actual value and not a lower limit, then the rest-frame brightness temperature of 3C 279 is quite high and limited by inverse Compton effects rather than equipartition. The parsec-scale morphology of 3C 279 consists of a bright, compact VLBI core, a jet component (C4) that moved from ~ 2 to ~ 3.5 mas from the core during the course of our monitoring, and an inner jet that extends from the core to a stationary component, C5, at ~ 1 mas from the core. Component C4 followed a curved path, and we reconstruct its three-dimensional trajectory using polynomial fits to its position versus time. Component C5 faded with time, possibly due to a previous interaction with C4 similar to interactions seen in simulations by Gómez et al. Components in the inner jet are relatively short lived and fade by the time they reach ~ 1 mas from the core. The components have different speeds and position angles from each other, but these differences do not match the differences predicted by the precession model of Abraham & Carrara. Although VLBI components were born about six months prior to each of the two observed γ-ray high states, the sparseness of the γ-ray data prevents a statistical analysis of possible correlations.

Subject headings: galaxies: active — galaxies: jets — quasars: individual (3C 279) —
　　　　　　　　radiation mechanisms: nonthermal — radio continuum: galaxies

On-line material: machine-readable table

1. INTRODUCTION

The quasar 3C 279 ($z = 0.536$) is one of the archetypal superluminal radio sources (Cotton et al. 1979). At γ-ray energies, the light curve of 3C 279 has been sampled intermittently since the launch of the Compton Observatory in 1991; it is one of the brightest EGRET quasars (Hartman et al. 1999). 3C 279 is also well known as an optically violent variable (OVV), with large and rapid outbursts (Webb et al. 1990). Strong variability on timescales shorter than one day is observed in high-energy bands (Wehrle et al. 1998; Lawson, McHardy, & Marscher 1999).

Correlations between the variability seen over the entire electromagnetic spectrum have proved elusive. Variability occurs on a variety of timescales, especially at high energies, and time sampling has been adequate to track the variations only at radio, millimeter, and X-ray bands, and as far as practicable in optical bands. There are strong theoretical

motivations for the search for correlations. The two-humped overall spectral energy distribution is most naturally explained as a combination of synchrotron radiation for the radio through optical-UV region, and inverse Compton emission at higher energies (Maraschi et al. 1994; Wehrle 1999). The synchrotron and inverse Compton emission is generally thought to be associated with a jet of relativistic electrons; however, the source of the seed photons for inverse Compton scattering is a matter of considerable debate (e.g., Maraschi, Ghisellini, & Celotti 1992; Sikora, Begelman, & Rees 1994). Distinguishing the differing mechanisms involves a full understanding of the time correlations in the different energy bands. A consensus is emerging that for GeV-peaked blazars, the seed photons upscattered to X-ray and γ-ray energies originate outside the jet (e.g., in the accretion disk or broad line region clouds) with a minor contribution from synchrotron photons (Urry 1999). A full understanding may have to await the next generation of γ-ray satellite observatories.

In the radio regime, the variability timescale is longer, and flux monitoring at 4.8, 8.4, and 14.5 GHz, complete with polarization data, has been obtained at the University of Michigan Radio Observatory (e.g., Aller et al. 1985). Monitoring at 22 and 37 GHz has been done at Metsähovi Observatory (Teräsranta et al. 1992, 1998). Less frequent monitoring has been performed at SEST (90 and 230 GHz) (Tornikoski et al. 1996) and at the JCMT (230 GHz) (Marscher et al. 1999).

The time variability of 3C 279's VLBI structure has been studied by several groups, beginning with the earliest days of the VLBI technique itself (Knight et al. 1971; Whitney et

[1] Jet Propulsion Laboratory, California Institute of Technology, 4800 Oak Grove Drive, Pasadena, CA 91109; Ann.E.Wehrle@jpl.nasa.gov, B. G. Piner@jpl.nasa.gov, Stephen.C.Unwin@jpl.nasa.gov.

[2] Department of Physics and Astronomy, Whittier College, 13406 E. Philadelphia Street, Whittier, CA 90608; gpiner@whittier.edu.

[3] Department of Physics and Astronomy, Pomona College, Claremont, CA 91711; azook@pomona.edu.

[4] Infrared Processing and Analysis Center, Jet Propulsion Laboratory, California Institute of Technology 100-22, Pasadena, CA 91125.

[5] Institute for Astrophysical Research, Boston University, 725 Commonwealth Avenue, Boston, MA 02215; marscher@bu.edu.

[6] Metsähovi Radio Observatory, Metsähovintie 114, 02540 Kylmälä, Finland; hte@kurp.hut.fi.

[7] Tuorla Observatory, Väisäläntie 20, FIN-21500 Piikkiö, Finland.

[8] Department of Physics, Turku University, FIN-20100 Turku, Finland; valtaoja@deneb.astro.utu.fi.

al. 1971; Cohen et al. 1971). Most of these observations were made using the ad hoc US and European VLBI Networks, with observations at intervals of about 1 yr (Unwin et al. 1989, hereafter U89; Carrara et al. 1993, hereafter C93; Abraham & Carrara 1998). With the advent of the NRAO Very Long Baseline Array[9] (VLBA), more frequent monitoring began in 1991, with an emphasis on higher radio frequencies (22 and 43 GHz). This paper presents results from this more frequent monitoring; preliminary results from this monitoring have been presented by Wehrle, Unwin, & Zook (1994), Wehrle et al. (1996), and Unwin et al. (1998). Polarization-sensitive VLBI images of 3C 279 have also been made by Leppänen, Zensus, & Diamond (1995), Cawthorne & Gabuzda (1996), Lister, Marscher, & Gear (1998), Lister & Smith (2000), and Homan & Wardle (1999) (who detect a significant component of circular polarization). Space VLBI observations at 5 and 1.6 GHz have been performed with the VLBI Space Observatory Programme (VSOP) since 1998; first results are reported by Piner et al. (2000).

The highest angular resolution achieved on 3C 279 is 50 μas, at 86 GHz (Rantakyrö et al. 1998), and VLBI fringes have been detected up to frequencies of 215 GHz (Krichbaum et al. 1997). In images from 1990 and 1992, Rantakyrö et al. (1998) showed a narrow string of components within about 1 mas of the core. Rantakyrö et al. speculate that most of the "missing" flux lies in a more extended jet which is resolved out by their 50 μas beam.

In this paper, we present the results of a long-term VLBI monitoring campaign on 3C 279. The data comprise VLBI images at 22 GHz over the period 1991–1997 (a total of 18 epochs) and at 43 GHz over the period 1995–1997 (10 epochs). In § 2 of this paper we present the VLBI observation series, explaining how the data were collected, calibrated, and analyzed. Section 3 presents the VLBI images. Section 4 discusses the superluminal motion visible in the image sequence and shows that different regions of the jet show qualitatively different evolution. Section 5 analyzes the flux density and spectral evolution of the radio core and components in the VLBI jet. We present our conclusions in § 6. In a subsequent paper (Piner et al. 2001, in preparation) we will combine synchrotron self-Compton models with our VLBI data and X-ray data to further constrain the jet kinematics. Throughout the paper we assume $H_0 = 70$ km s^{-1} Mpc^{-1} and $q_0 = 0.1$, and component speeds measured by others have been expressed in these terms. With these assumptions, 1 mas corresponds to a linear distance of 5.8 pc, and a proper motion of 1 mas yr^{-1} corresponds to an apparent speed of $29c$.

2. VLBI OBSERVATIONS

We have observed 3C 279 at 22 GHz since the mid 1980s, and at 43 GHz since 1995. Our first experiments used the Global VLBI Network which was composed of nonidentical antennas at various observatories. The data through 1994 were recorded in Mark II mode with 2 MHz bandwidth, followed by correlation at the Caltech/JPL Block II Correlator. The Global Network usually had three observing sessions per year of which two (at most) included 22 GHz. During those sessions, seven antennas were able to

mount 22 GHz receivers. In 1991, we added the first antennas in the new NRAO VLBA. By the mid 1990s, we used the VLBA alone with 32 MHz bandwidth recorded on tapes correlated at the VLBA Correlator in Socorro, New Mexico. We added 43 GHz to our monitoring starting in 1995. Some of the later maps were made in "snapshot" mode, while others were made with full (u, v) tracks. Most of the full-track observations since 1995 were done with alternating scans at 22 and 43 GHz, and sometimes a lower frequency. Results from this monitoring program prior to 1991 are discussed by U89 and C93. The data obtained during the more frequent monitoring since 1991 are discussed in this paper; these VLBI observations are listed in Table 1. Since the end of our monitoring program in 1997, 3C 279 has been part of a VLBA polarization monitoring program described by Marchenko et al. (1999).

Images from some of the epochs listed in Table 1 have appeared in various conference proceedings (e.g., Wehrle et al. 1994, 1996; Unwin et al. 1998). In many cases, we have reanalyzed the original data, and obtained significantly improved images. The biggest improvement was in correcting station-based calibration errors (and deletion of bad data in some cases); the interactive self-calibration, display, and imaging package DIFMAP (Shepherd, Pearson, & Taylor 1994) was the key to realizing these improvements. For some of the epochs listed in Table 1, observations at lower frequencies were made as well, but since these observations contribute little to following source structure changes (because of their lower resolution), discussion of these observations will be deferred until the discussion of the broadband spectrum in Piner et al. (2001, in preparation). Beginning in 1995 many of our observations recorded dual circular polarization. In this paper, we discuss only the total intensity images formed from these observations.

The data were fringe-fitted in AIPS, then exported to the Caltech DIFMAP package (Shepherd et al. 1994) for amplitude and phase calibration, editing, and mapping. The 22 GHz data required particular attention to amplitude calibration because water vapor in Earth's atmosphere absorbs at this frequency. Normal self-calibration does not take care of this problem if it is cloudy at most antennas because there are insufficient crossing points in the (u, v) plane for sources that are nearly equatorial (like 3C 279); moreover, the problem is worse for antennas that are located far from the mainland array such as Saint Croix (which is nearly at sea level) or Mauna Kea (which observes at low elevation angles). We compared the 22 GHz monitoring data from Metsähovi (where only the data obtained with dry observing conditions are accepted) with the flux density measured on the shortest VLBI baselines, and applied an initial scaling factor of order 1.1–1.3 to antenna gains for stations affected by cloudy weather. We estimate that 3C 279 has about 1 Jy in 22 GHz emission which is too diffuse to be sampled by the shortest spacings in the (u, v) plane. In most cases, we chose an epoch with good weather to map and model fit, then used the input model to initiate the mapping-self-calibration sequence for adjacent epochs with bad weather. Data from antennas obtained during snow or rain were flagged after we found that they had significant adverse effects on the images.

The amplitude calibration of the 43 GHz data was compared with the 37 GHz monitoring flux densities from Metsähovi. In nearly all cases, the fluxes agreed to within

TABLE 1
VLBI OBSERVATIONS

Epoch	Experiment Name	VLBA Antennas[a]	Other antennas[b]	Bandwidth (MHz)	Obs. Time[c] (minutes)	Frequencies[d] (GHz)	Polarization
1991 Jun 24	GU2B	Fd, Kp, La, Nl, Pt	Eb, Gb, Hs, Mc, Nt, On, Ov, Y1	2	973	22	LCP
1992 Jun 14	GW6B	Br, Fd, Kp, La, Nl, Ov, Pt	Eb, Gb, Hs, Mc, Mh, On, Y1	2	703	22	LCP
1992 Nov 10	GW6C	Br, Hn, Kp, La, Nl, Ov, Pt	Gb, Mc, Mh, Nt, On, Y1	2	485	22	LCP
1993 Feb 17	GW008	Br, Hn, Kp, Ov, Pt, Sc	Eb, Mc, Mh, Y1	2	521	22	LCP
1993 Nov 8	BM030	Br, Hn, Mk, Nl, Ov, Pt	...	2	115	22	LCP
1994 Mar 2	GW011A	Br, Fd, Hn, Kp, La, Mk, Nl, Ov, Sc	Eb, Gb, Mc, Mh, Nt, On, Y1	14	755	22	LCP
1994 Jun 12	BM032A	Hn, Mk, Nl, Ov, Pt, Sc	...	2	96	22	LCP
1994 Sep 21	GW011B	Br, Fd, Hn, Kp, La, Nl, Ov, Pt, Sc	Y1	14	433	22	LCP
1995 Jan 4	BB025	All	...	16	32	22	Dual
1995 Feb 25	BM038	All	...	16	25, 45	22, 43	Dual
1995 Mar 19	GW013B	All	...	16	297, 297	22, 43	Dual
1996 Jan 7	GW013C	All	...	32	311, 311	22, 43	LCP
1996 May 4	BM063	All	...	32	58	43	Dual
1996 May 13	BW026	All	...	16	278	22	Dual
1996 Jun 9	BW026B	All	...	16	278, 278	22, 43	Dual
1996 Nov 24	BM072	All	...	8	27	43	Dual
1997 Jan 15	BW026D	All	...	16	256, 256	22, 43	Dual
1997 Mar 29	BW031A	Br, Fd, Hn, Kp, La, Mk, Ov, Pt, Sc	...	16	190, 190	22, 43	Dual
1997 Jul 16	BW031B	All	...	16	190, 190	22, 43	Dual
1997 Nov 16	BW031C	Br, Fd, Kp, Mk, Nl, Ov, Pt, Sc	...	16	168, 167	22, 43	Dual

[a] (Br) Brewster, WA ; (Fd) Fort Davis, TX ; (Hn) Hancock, NH ; (Kp) Kitt Peak, AZ ; (La) Los Alamos, NM ; (Mk) Mauna Kea, HI ; (Nl) North Liberty, IA ; (Ov) Owens Valley, CA ; (Pt) Pie Town, NM ; (Sc) St. Croix, US Virgin Islands.

[b] Antenna locations and sizes are as follows: (Eb) Effelsberg, Germany, 100 m; (Gb) Green Bank, WV, 43 m; (Hs) Haystack, MA, 37 m; (Mc) Medicina, Italy, 32 m; (Mh) Metsähovi, Finland, 14 m; (Mp) Maryland Point, MD, 26 m; (Nt) Noto, Italy, 32 m; (On) Onsala, Sweden, 20 m; (Ov) Owens Valley, CA, 40 m; (Y1) one antenna of the VLA, Socorro, NM, 25 m.

[c] Two numbers indicate time on source at 22 and 43 GHz, respectively.

[d] Lower observed frequencies are not listed here since they are not discussed in this paper.
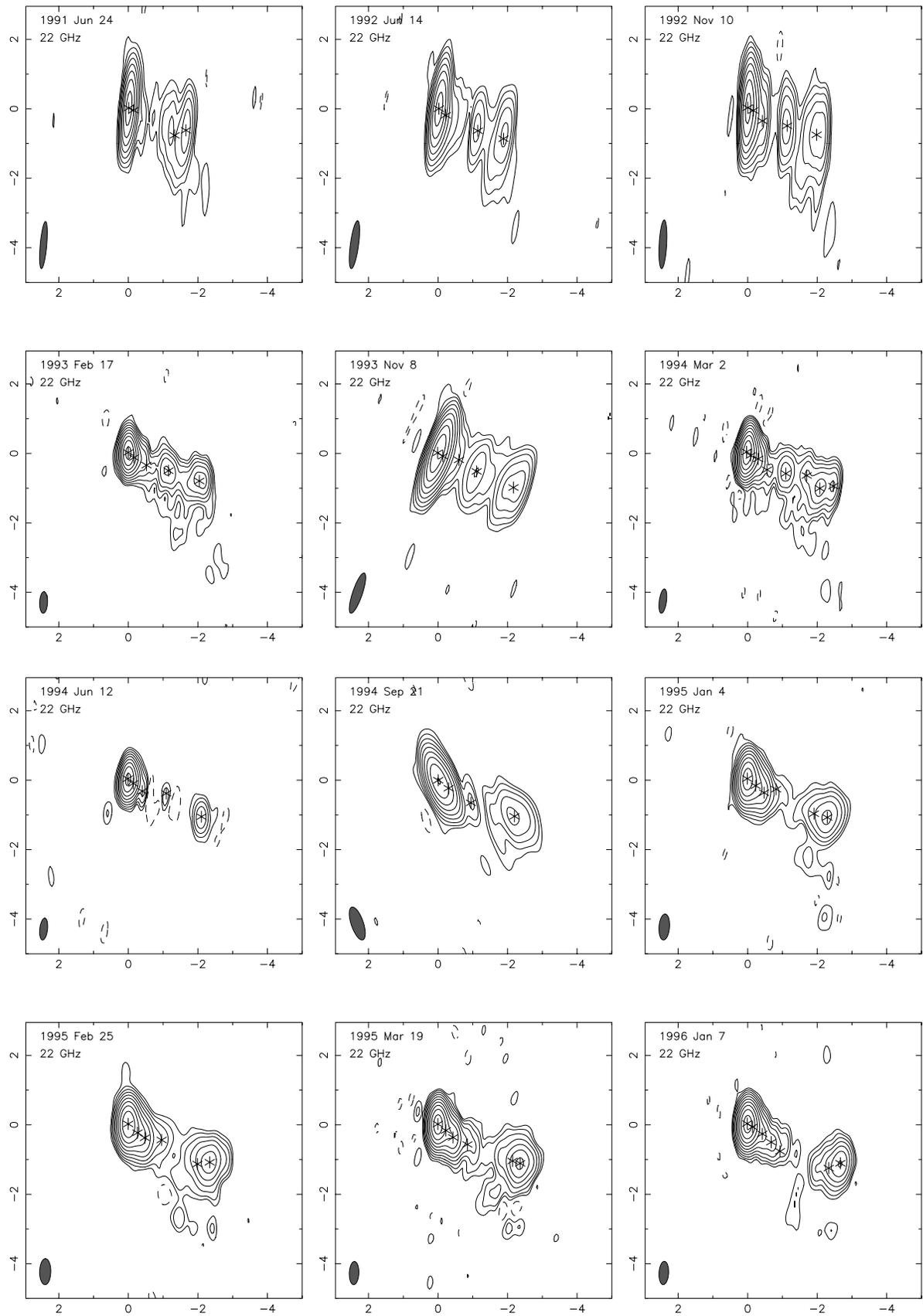
FIG. 1.—22 GHz uniformly weighted images of 3C 279 from the 18 epochs listed in Table 1. The axes are labeled in milliarcseconds. Parameters of the images are given in Table 2. Model-fit Gaussian positions are marked with asterisks. The model-fit Gaussians are identified in Table 3.
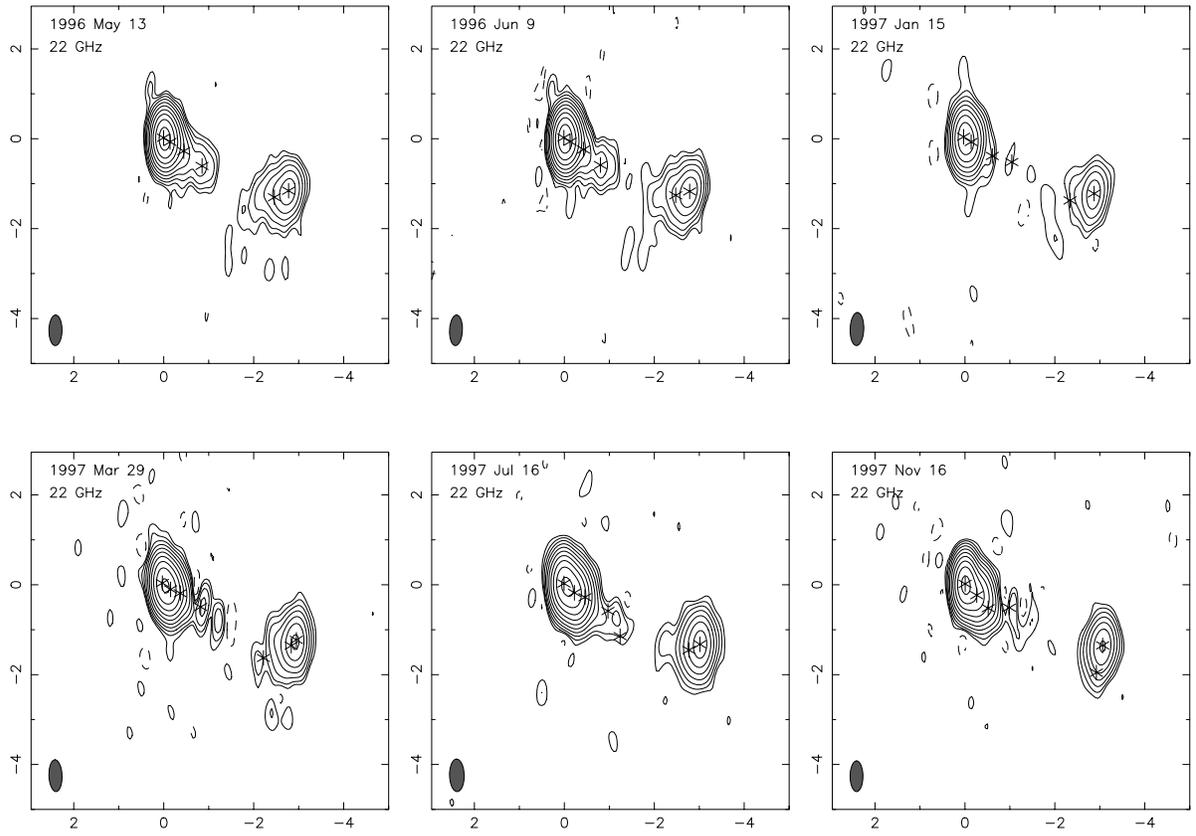
FIG. 1.—Continued
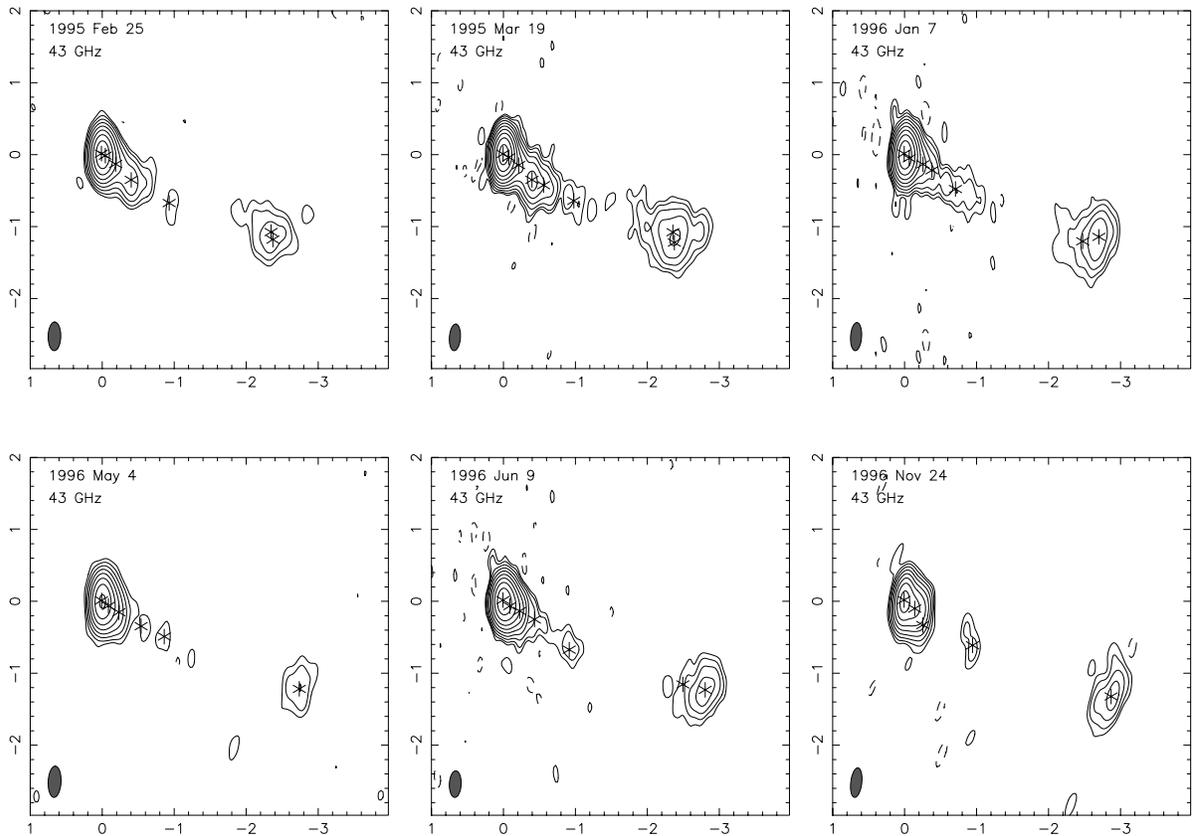
FIG. 2.—43 GHz uniformly weighted images of 3C 279 from the 10 epochs listed in Table 1. The axes are labeled in milliarcseconds. Parameters of the images are given in Table 2. Model-fit Gaussian positions are marked with asterisks. The model-fit Gaussians are identified in Table 3.
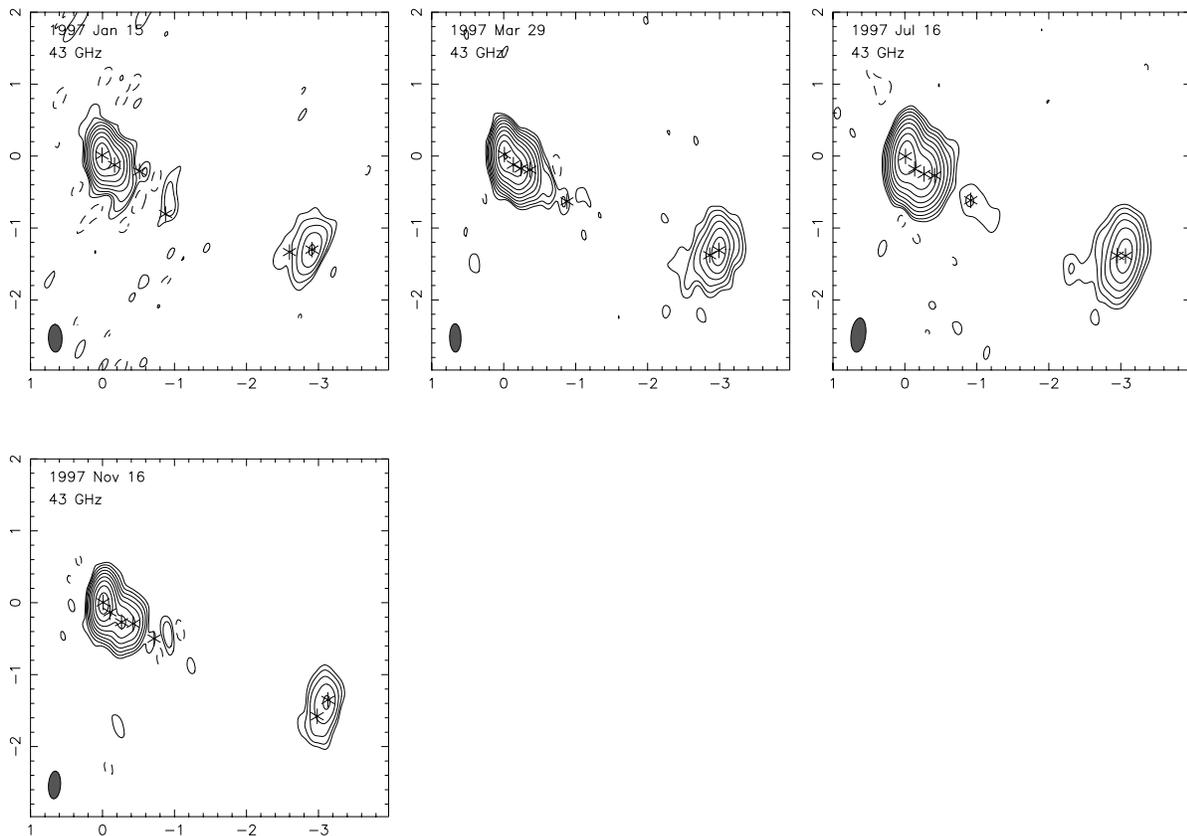
FIG. 2.—*Continued*

20%; discrepant antennas were scaled accordingly. Self-calibration enables us to make reliable images for the purpose of tracking changes in the source structure; however, the scale factors applied render the overall flux scale somewhat uncertain. This limits our ability to track the flux density evolution of individual components at better than about a 10% level.

3. VLBI IMAGING RESULTS

Figure 1 shows the 18 images at 22 GHz of 3C 279 from the epochs listed in Table 1, and Figure 2 shows the 10 images at 43 GHz. The images are shown with uniform weighting (uvweight = 2, 0 in DIFMAP) to maximize the resolution. Even though this produces an image with lower dynamic range, the high resolution is important for distinguishing components in the inner milliarcsecond. The parameters of these images are listed in Table 2. Model-fit Gaussian positions are marked with asterisks on the images. The model-fitting results are discussed in § 4.1.

The parsec-scale morphology of 3C 279 during the years 1991–1997 consists of the bright compact core, a bright secondary component at a position angle of −114°, which moves outward from about 2 mas to about 3.5 mas from the core during the observed time range, and an inner jet that extends from the core out to about 1 mas. We identify the bright secondary component with the component C4 seen previously in our monitoring (U89; C93), and subsequently by many other authors. In the earlier images, C4 is connected to the inner jet emission, but in the later images it is clearly separated, with a gap in emission between the 1 mas point and C4. The region interior to 1 mas is complex, with multiple components forming, moving out, and fading on

timescales of several years. Component C4 is resolved and has significant internal structure, with multiple Gaussians often required to model it (see § 4.1). The higher dynamic range images (e.g., the 22 GHz images from 1993 February 17 and 1994 March 2) show extended, diffuse emission to the southwest of the main jet. This extended, diffuse emission has a position angle of about −140° to −150°, similar to that of the larger-scale VLBI jet seen at lower frequencies (Piner et al. 2000), and the kiloparsec-scale jet seen with the VLA and MERLIN (de Pater & Perley 1983; Pilbratt, Booth, & Porcas 1987; Akujor et al. 1994). No counterjet is detected, and the limit placed on the jet/counterjet brightness ratio is about 100 : 1 at the distance of C4.

4. MOTION OF JET COMPONENTS

4.1. *Identification of Components by Model Fitting*

We used the "modelfit" routine in DIFMAP to fit Gaussians to the visibility data for each epoch. These Gaussian models are listed in Table 3. Our procedure was to replace all CLEAN components with a collection of circular Gaussians, letting the circular Gaussians become elliptical if required to fit the visibility data and residual map. All regions of the jet could be successfully modeled with circular Gaussians with the exception of the resolved jet component C4, which required one or more elliptical Gaussians at some epochs. Use of circular Gaussians has the advantage that it prevents representation of one or more jet components by a single, long, elliptical Gaussian.

The Gaussian models are identified with named jet components in Table 3. In all we identify a total of eight distinct jet components that we name C4, C5, C5a, C6, C7, C7a, C8, and C9 from the outermost component inward. A few

TABLE 2

PARAMETERS OF THE IMAGES

Epoch	Frequency (GHz)	Beam[a]	Total Flux[b] (Jy)	CLEAN Flux (Jy)	Peak Flux (Jy beam^{-1})	Lowest Contour[c] (mJy beam^{-1})	Contours[d] (Multiples of Lowest Contour)
1991 Jun 24	22	1.36, 0.19, −5.0	15.7	15.3	9.4	50.5	1...2^7
1992 Jun 14	22	1.39, 0.24, −7.6	14.1	14.0	9.3	51.4	1...2^7
1992 Nov 10	22	1.40, 0.21, −3.1	15.2	15.3	9.6	28.6	1...2^8
1993 Feb 17	22	0.62, 0.23, −2.3	15.8	16.2	10.6	16.2	1...2^9
1993 Nov 8	22	1.22, 0.28, −18.7	19.9	20.2	15.3	31.9	1...2^8
1994 Mar 2	22	0.71, 0.21, −7.7	20.5	20.0	12.9	13.1	1...2^9
1994 Jun 12	22	0.63, 0.22, −6.4	...	19.7	15.1	47.0	1...2^8
1994 Sep 21	22	0.99, 0.35, 18.7	...	20.1	14.9	56.7	1...2^8
1995 Jan 4	22	0.75, 0.30, −4.3	18.3	18.6	12.1	29.4	1...2^8
1995 Feb 25	22	0.75, 0.32, −0.9	18.6	18.5	12.3	23.9	1...2^9
1995 Mar 19	22	0.67, 0.27, −2.1	19.2	18.9	12.3	14.7	1...2^9
1996 Jan 7	22	0.67, 0.28, −3.3	20.4	19.7	14.1	18.6	1...2^9
1996 May 13......	22	0.68, 0.29, −0.6	24.1	23.5	17.6	23.3	1...2^9
1996 Jun 9	22	0.68, 0.29, −2.6	28.4	27.7	20.9	22.4	1...2^9
1997 Jan 15	22	0.74, 0.30, −2.0	24.5	24.9	17.6	73.0	1...2^7
1997 Mar 29	22	0.71, 0.29, 2.1	24.8	23.8	14.9	25.7	1...2^9
1997 Jul 16........	22	0.72, 0.33, 1.4	27.6	25.1	14.4	22.9	1...2^9
1997 Nov 16	22	0.68, 0.29, 0.1	35.4	34.7	21.9	33.6	1...2^9
1995 Feb 25	43	0.40, 0.18, −0.9	19.5	18.4	13.5	55.6	1...2^7
1995 Mar 19	43	0.37, 0.15, −4.0	19.6	18.6	13.6	18.0	1...2^9
1996 Jan 7	43	0.39, 0.15, −3.7	20.8	19.9	14.6	28.9	1...2^8
1996 May 4	43	0.44, 0.18, −2.7	22.4	22.5	17.1	117	1...2^7
1996 Jun 9	43	0.37, 0.16, −2.5	26.4	24.6	17.4	35.1	1...2^8
1996 Nov 24	43	0.41, 0.15, −6.7	21.3	22.3	12.7	69.2	1...2^7
1997 Jan 15	43	0.39, 0.19, 1.8	21.9	21.5	14.2	60.7	1...2^7
1997 Mar 29	43	0.40, 0.16, 1.1	21.8	19.6	9.0	16.9	1...2^9
1997 Jul 16........	43	0.48, 0.20, −7.2	20.9	20.0	10.4	21.6	1...2^8
1997 Nov 16	43	0.39, 0.17, −3.9	33.7	32.7	21.0	55.5	1...2^8

[a] Numbers given for the beam are the FWHMs of the major and minor axes in mas, and the position angle of the major axis in degrees. The beam has been synthesized using uniform weighting.

[b] Single-dish flux from Metsähovi at 22 or 37 GHz. Absent entries indicate periods of no observing.

[c] The lowest contour is set to be three times the rms noise in the full image.

[d] Contour levels are represented by the geometric series 1...2^n, e.g., for $n = 5$ the contour levels would be $\pm 1, 2, 4, 8, 16, 32$.

words must be said about the naming convention chosen for the jet components. In all cases, we have tried to be consistent with naming schemes adopted by other authors, and this has sometimes required the addition of a component name with the "a" suffix in cases where a component was missed due to the sporadic single-epoch observations by various authors. Note also that there are two naming conventions in use for jet components in 3C 279. The component named "C5" by C93 and Abraham & Carrara (1998) is not the same component referred to as "C5" by Wehrle et al. (1994), Leppänen et al. (1995), and Lister et al. (1998). We have not detected the "C5" component reported by C93 and Abraham & Carrara (1998), so in this paper we adopt the naming scheme of Wehrle et al. (1994), Leppänen et al. (1995), and Lister et al. (1998).

We caution that Gaussian model fitting does not always produce unique results, especially for regions of nearly continuous jet emission. Blending of jet components into single Gaussians can be a problem at lower resolutions. Component C5 is stationary at about 1 mas from the core, and as moving jet components approach C5, the distinction between whether a given Gaussian model represents C5 or the approaching, moving component becomes ambiguous. Three closely spaced components in the inner jet (C7a, C8, and C9) are detected in the 43 GHz data. The 22 GHz

model fits tend to represent these three jet components with only two Gaussians, so further discussion of C7a, C8, and C9 is derived from the 43 GHz model fits. The bright jet component C4 is detected at all epochs, and as it moves out its internal structure becomes more complex, and more than one Gaussian is frequently required to represent it. These multiple-Gaussian fits to C4 nearly always take the form of a brighter, more compact leading edge at a more northerly position angle, and a fainter, more diffuse trailing Gaussian at a more southerly position angle. The position of the brightest Gaussian is used to represent the position of C4, these Gaussians are marked with asterisks in Table 3. At two epochs (1994 March 2 and 1997 March 29) three Gaussians are required to represent C4 (see Table 3). The sharp leading edge of this component is suggestive of a working surface or shock front. The polarization observations of Leppänen et al. (1995), Lister et al. (1998), and Homan & Wardle (1999) show that C4 has a magnetic field transverse to the jet, also indicative of a shock front.

4.2. Apparent Radial Motion

In this section we discuss the apparent radial motion of the jet components identified in the previous section. All of the jet components display apparent superluminal motions with the exception of C5, which appears stationary at about

TABLE 3
GAUSSIAN MODELS

Epoch	Frequency (GHz)	Component[a] ID	S[b] (Jy)	r[c] (mas)	PA[c] (deg)	a[d] (mas)	b/a	Φ[e] (deg)
1991 Jun 24	22	Core	9.89	...	...	0.10	1.00	...
		C5a	1.82	0.15	−114.9	0.25	1.00	...
		C5	2.18	1.54	−120.8	0.87	1.00	...
		C4	1.42	1.77	−111.3	0.14	1.00	...
1992 Jun 14	22	Core	9.82	...	...	0.11	1.00	...
		C5a	1.29	0.28	−133.6	0.17	1.00	...
		C5	1.33	1.29	−119.6	0.95	1.00	...
		C4	1.52	2.05	−115.0	0.27	1.00	...
1992 Nov 10......	22	Core	8.93	...	...	0.03	1.00	...
		C6	2.52	0.18	−117.0	0.14	1.00	...
		C5a	0.60	0.57	−131.9	0.22	1.00	...
		C5	0.98	1.25	−114.7	0.27	1.00	...
		C4	2.14	2.13	−111.5	0.46	1.00	...
1993 Feb 17	22	Core	10.86	...	...	0.09	1.00	...
		C6	1.73	0.22	−132.1	0.19	1.00	...
		C5a	0.57	0.64	−124.8	0.35	1.00	...
		C5	1.11	1.27	−114.4	0.33	1.00	...
		C4	1.80	2.20	−111.9	0.44	1.00	...
1993 Nov 8	22	Core	14.14	...	...	0.07	1.00	...
		C6/7	3.57	0.18	−123.2	0.19	1.00	...
		C5a	0.21	0.65	−108.6	0.00	1.00	...
		C5	0.95	1.25	−115.6	0.39	1.00	...
		C4	1.87	2.40	−114.7	0.53	1.00	...
1994 Mar 2	22	Core	12.31	...	...	0.08	1.00	...
		C7	3.80	0.16	−132.0	0.11	1.00	...
		C6	0.82	0.39	−121.6	0.11	1.00	...
		C5a	0.23	0.78	−131.5	0.24	1.00	...
		C5	0.62	1.29	−119.0	0.34	1.00	...
		C4	0.38	1.86	−111.5	0.27	1.00	...
		C4*	1.26	2.35	−116.6	0.33	1.00	...
		C4	0.45	2.68	−111.6	0.07	1.00	...
1994 Jun 12	22	Core	15.53	...	...	0.10	1.00	...
		C7	3.36	0.20	−131.2	0.15	1.00	...
		C6	0.32	0.55	−130.9	0.00	1.00	...
		C5	0.22	1.18	−110.9	0.17	1.00	...
		C4	1.20	2.38	−117.3	0.28	1.00	...
1994 Sep 21	22	Core	14.54	...	...	0.10	1.00	...
		C6/7	2.92	0.37	−127.5	0.13	1.00	...
		C5	0.51	1.14	−124.6	0.90	1.00	...
		C4	2.24	2.42	−115.4	0.59	1.00	...
1995 Jan 4	22	Core	12.07	...	...	0.07	1.00	...
		C7	2.66	0.32	−130.6	0.12	1.00	...
		C6	1.11	0.63	−130.1	0.00	1.00	...
		C5a	0.23	0.88	−110.3	0.37	1.00	...
		C4	0.84	2.17	−117.8	1.04	1.00	...
		C4*	1.73	2.56	−115.9	0.37	1.00	...
1995 Feb 25	22	Core	12.55	...	...	0.09	1.00	...
		C7	1.76	0.37	−133.5	0.00	1.00	...
		C6	1.39	0.62	−129.9	0.18	1.00	...
		C5a	0.27	1.07	−115.7	0.39	1.00	...
		C4	0.78	2.30	−120.1	0.94	1.00	...
		C4*	1.75	2.59	−115.2	0.38	1.00	...
1995 Mar 19......	22	Core	12.67	...	...	0.08	1.00	...
		C7	1.47	0.29	−128.1	0.07	1.00	...
		C6	1.81	0.58	−131.1	0.17	1.00	...
		C5a	0.43	1.03	−124.5	0.50	1.00	...
		C4	0.97	2.40	−116.3	0.86	1.00	...
		C4*	1.58	2.62	−115.5	0.34	1.00	...
1996 Jan 7	22	Core	13.19	...	...	0.06	1.00	...
		C7a/8	2.86	0.18	−122.4	0.14	1.00	...
		C7	0.60	0.53	−124.4	0.00	1.00	...
		C6	0.49	0.88	−127.7	0.19	1.00	...
		C5	0.16	1.24	−130.2	0.08	1.00	...
		C4	0.92	2.67	−118.7	0.64	1.00	...

TABLE 3—*Continued*

Epoch	Frequency (GHz)	Component[a] ID	S[b] (Jy)	r[c] (mas)	PA[c] (deg)	a[d] (mas)	b/a	Φ[e] (deg)
		C4*	1.47	2.91	−113.1	0.22	1.00	...
1996 May 13......	22	Core	15.37	...	...	0.06	1.00	...
		C7a/8	4.92	0.17	−123.1	0.11	1.00	...
		C7	0.59	0.54	−123.6	0.14	1.00	...
		C6	0.39	1.06	−126.3	0.32	1.00	...
		C4	0.85	2.80	−118.3	0.64	1.00	...
		C4*	1.35	3.02	−113.0	0.22	1.00	...
1996 Jun 9	22	Core	17.25	...	...	0.04	1.00	...
		C7a/8	7.00	0.17	−123.0	0.10	1.00	...
		C7	0.54	0.51	−121.3	0.00	1.00	...
		C6	0.50	1.02	−127.0	0.38	1.00	...
		C4	0.92	2.80	−117.3	0.67	1.00	...
		C4*	1.51	3.04	−113.2	0.36	0.26	−41.4
1997 Jan 15	22	Core	13.44	...	...	0.00	1.00	...
		C8	8.23	0.20	−124.7	0.12	1.00	...
		C7	0.27	0.77	−123.7	0.25	1.00	...
		C5	0.10	1.21	−117.7	0.08	1.00	...
		C4	0.73	2.76	−120.9	0.92	1.00	...
		C4*	2.29	3.17	−113.5	0.29	0.34	−47.9
1997 Mar 29	22	Core	10.62	...	...	0.00	1.00	...
		C8/9	9.18	0.23	−127.7	0.10	1.00	...
		C7a	0.80	0.46	−119.6	0.00	1.00	...
		C7	0.32	1.00	−121.9	0.50	1.00	...
		C4	0.26	2.80	−126.6	0.74	1.00	...
		C4	1.09	3.19	−115.9	0.36	1.00	...
		C4*	1.60	3.24	−113.0	0.30	0.14	−26.1
1997 Jul 16........	22	Core	11.37	...	...	0.04	1.00	...
		C8/9	9.62	0.31	−131.9	0.17	1.00	...
		C7a	0.73	0.56	−123.3	0.00	1.00	...
		C5	0.10	1.15	−122.1	0.15	1.00	...
		C5a?	0.07	1.71	−133.2	0.11	1.00	...
		C4	0.48	3.15	−118.1	0.78	1.00	...
		C4*	2.72	3.31	−114.1	0.32	0.57	−23.4
1997 Nov 16	22	Core	21.36	...	...	0.08	1.00	...
		C8/9	9.46	0.36	−134.3	0.26	1.00	...
		C7/7a	0.58	0.75	−136.6	0.00	1.00	...
		C5	0.18	1.12	−118.3	0.00	1.00	...
		C4*	3.10	3.35	−114.1	0.25	0.78	−56.9
		C4	0.33	3.53	−124.1	0.00	1.00	...
1995 Feb 25......	43	Core	9.47	...	...	0.00	1.00	...
		C7a	5.34	0.06	−117.5	0.08	1.00	...
		C7	0.92	0.25	−126.3	0.10	1.00	...
		C6	1.27	0.55	−131.4	0.21	1.00	...
		C5	0.20	1.17	−126.2	0.20	1.00	...
		C4*	1.03	2.60	−114.8	0.57	1.00	...
		C4	0.28	2.67	−116.7	0.11	1.00	...
1995 Mar 19	43	Core	12.57	...	...	0.03	1.00	...
		C7a	2.78	0.09	−121.3	0.05	1.00	...
		C7	0.67	0.27	−125.8	0.11	1.00	...
		C6	0.85	0.54	−131.9	0.10	1.00	...
		C5a	0.42	0.71	−127.7	0.19	1.00	...
		C5	0.17	1.18	−123.6	0.37	1.00	...
		C4*	1.08	2.60	−114.8	0.51	1.00	...
		C4	0.24	2.68	−117.4	0.14	1.00	...
1996 Jan 7	43	Core	12.43	...	...	0.04	1.00	...
		C8	4.89	0.10	−132.5	0.08	1.00	...
		C7a	0.69	0.30	−119.7	0.15	1.00	...
		C7	0.11	0.45	−121.1	0.00	1.00	...
		C6	0.49	0.87	−124.7	0.44	1.00	...
		C4	0.59	2.76	−116.2	0.62	1.00	...
		C4*	0.88	2.94	−113.2	0.45	0.40	−15.0
1996 May 4	43	Core	15.01	...	...	0.03	1.00	...
		C8	4.63	0.12	−128.9	0.05	1.00	...
		C7a	1.32	0.29	−124.4	0.06	1.00	...
		C7	0.19	0.66	−123.2	0.09	1.00	...
		C6	0.23	1.01	−120.0	0.06	1.00	...

305

TABLE 3—*Continued*

Epoch	Frequency (GHz)	Component[a] ID	S[b] (Jy)	r[c] (mas)	PA[c] (deg)	a[d] (mas)	b/a	Φ[e] (deg)
		C4	1.14	3.01	−114.1	0.31	1.00	...
1996 Jun 9	43	Core	15.67	...	...	0.05	1.00	...
		C8	6.16	0.13	−131.1	0.08	1.00	...
		C7a	1.21	0.28	−123.2	0.05	1.00	...
		C7	0.25	0.51	−121.6	0.22	1.00	...
		C5	0.19	1.15	−126.8	0.14	1.00	...
		C4	0.29	2.76	−115.1	0.86	0.46	−34.0
		C4*	0.98	3.08	−114.0	0.40	0.42	−35.8
1996 Nov 24	43	Core	11.44	...	...	0.05	1.00	...
		C8	8.84	0.19	−128.6	0.20	1.00	...
		C7a	0.37	0.43	−143.2	0.00	1.00	...
		C5	0.24	1.14	−123.5	0.20	1.00	...
		C4	1.78	3.17	−115.0	0.22	1.00	...
1997 Jan 15	43	Core	13.34	...	...	0.03	1.00	...
		C8	6.04	0.22	−127.7	0.12	1.00	...
		C7/7a	0.16	0.57	−113.3	0.00	1.00	...
		C5	0.16	1.20	−132.8	0.04	1.00	...
		C4	0.20	2.93	−117.3	0.00	1.00	...
		C4*	1.68	3.20	−114.2	0.38	0.10	−34.4
1997 Mar 29	43	Core	8.80	...	...	0.06	1.00	...
		C9	4.05	0.19	−138.7	0.07	1.00	...
		C8	4.02	0.30	−130.1	0.08	1.00	...
		C7a	0.81	0.41	−121.0	0.15	1.00	...
		C5	0.18	1.09	−126.9	0.30	1.00	...
		C4	0.64	3.18	−116.2	0.67	1.00	...
		C4*	1.28	3.26	−114.1	0.25	0.57	−24.7
1997 Jul 16	43	Core	10.21	...	...	0.05	1.00	...
		C9	2.62	0.22	−143.7	0.00	1.00	...
		C8	4.09	0.36	−133.3	0.04	1.00	...
		C7a	0.97	0.48	−123.4	0.07	1.00	...
		C5	0.08	1.09	−123.9	0.18	1.00	...
		C4	0.73	3.25	−115.1	0.74	0.33	−14.1
		C4*	1.26	3.36	−114.4	0.24	0.59	−12.3
1997 Nov 16	43	Core	21.06	...	...	0.05	1.00	...
		C9	3.39	0.17	−145.7	0.04	1.00	...
		C8	4.19	0.38	−137.2	0.08	1.00	...
		C7a	1.81	0.51	−125.5	0.08	1.00	...
		C7	0.14	0.87	−125.5	0.00	1.00	...
		C4	0.90	3.37	−118.0	0.29	1.00	...
		C4*	1.31	3.40	−113.5	0.18	1.00	...

[a] Multiple IDs listed for a single Gaussian indicate a blending of jet components. Jet component C4 sometimes required multiple Gaussians to fit. The brightest Gaussian making up C4 is marked with an asterisk, and its position is used as the position of C4.

[b] Flux density in Janskys.

[c] r and PA are the polar coordinates of the center of the Gaussian relative to the presumed core. Position angle is measured from north through east.

[d] a and b are the FWHM of the major and minor axes of the Gaussian.

[e] Position angle of the major axis measured from north through east.

1.2 mas from the core, and C9, which is present in the last three epochs at 43 GHz at about 0.2 mas from the core. The moving components interior to C5 tend to fade and disappear below our detection limit as they approach C5, although there are some indications that they may remain barely detectable beyond this point (e.g., the emission beyond C5 in the 1997 November 16 map at 22 GHz). Three of the inner jet components (C5a, C6, and C7) have undergone this behavior during our monitoring.

Motion of jet components in 3C 279 can be seen directly from the images. Figures 3 and 4 show a selection of images at 22 and 43 GHz, respectively. Only a selection of images are shown because there are too many images to fit on a single page. These images are presented as time-series mosaics with dotted lines indicating the best fits to motion

at constant speed for the model-fit Gaussians. Animations made from the entire sequences of images may be obtained from ftp://sgra.jpl.nasa.gov/pub/users/glenn/3c279_22ghz.mpeg and 3c279_43ghz.mpeg.

The measured model-fit Gaussian positions versus time are shown in Figures 5a and 5b for the 22 and 43 GHz model fits, respectively. Error bars on the Gaussian positions have been set to be proportional to the beam size and inversely proportional to the square root of the dynamic range of the component detection (defined here as the uniform-Gaussian surface brightness divided by the rms residual surface brightness), and normalized to be one-quarter of a beam at a dynamic range of 200 by observing the scatter in the Gaussian positions. Although the error may formally be inversely proportional to the dynamic
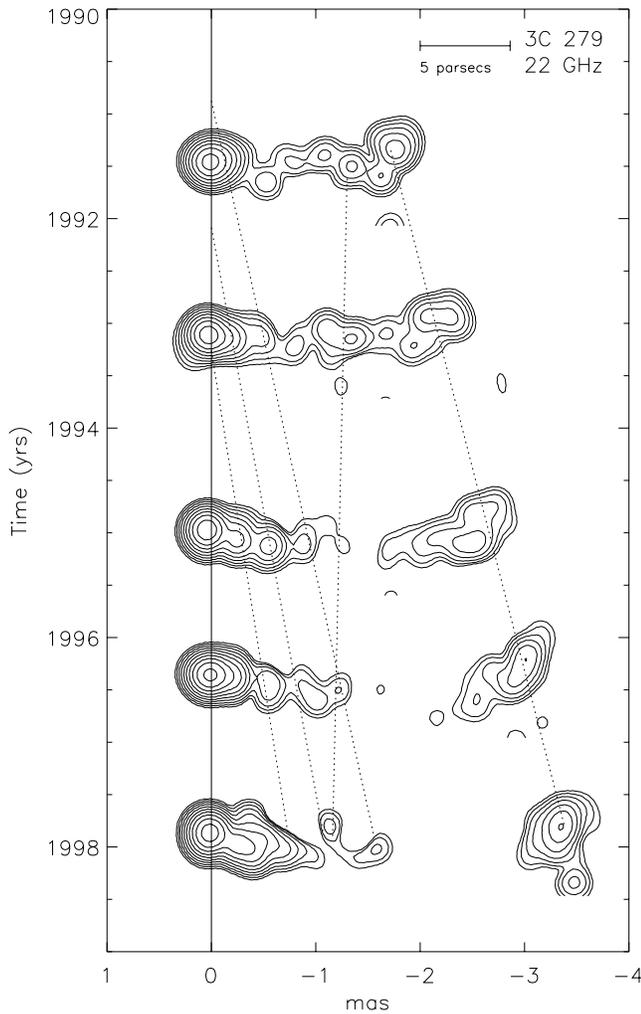
FIG. 3.—Time-series mosaic of a selection of 22 GHz VLBI images of 3C 279. Epochs 1991 June 24, 1993 February 17, 1994 September 21, 1996 May 13, and 1997 November 16 are shown. The images have been restored with a circular 0.2 mas beam without residuals and rotated 25° counter-clockwise. The lowest contour is 25 mJy beam^{-1}; subsequent contours are a factor of two higher than the previous contour. The solid line indicates the position of the presumed stationary core. The dotted lines represent the best fits to the model-fit Gaussian positions vs. time from Fig. 5a. From right to left these lines represent C4, C5, C5a, C6, and C7. Some lines have been extended before and after model-fit detections to show speculative zero-separation epochs and later positions.

FIG. 4.—Time-series mosaic of a selection of 43 GHz VLBI images of 3C 279. Epochs 1995 March 19, 1996 January 7, 1996 June 9, 1997 March 29, and 1997 November 16 are shown. The images have been restored with a circular 0.15 mas beam without residuals and rotated 25° counter-clockwise. The lowest contour is 25 mJy beam^{-1}; subsequent contours are a factor of two higher than the previous contour. The solid line indicates the position of the presumed stationary core. The dotted lines represent the best fits to the model-fit Gaussian positions vs. time from Fig. 5b. From right to left these lines represent C4, C5, C6, C7, C7a, C8, and C9. Some lines have been extended before model-fit detections to show speculative zero-separation epochs.

range (rather than the square root) (e.g., Fomalont 1985; Reid & Moran 1988; Condon 1997), the range in component surface brightnesses in 3C 279 is so large (of order 1000 between C8 and C5) that this produces an extremely large range in errors that does not empirically agree with the scatter in the model-fit positions. Effects other than visibility errors [e.g., (u, v) coverage effects, calibration errors, and interactions among multiple model components] presumably dominate at the higher surface brightnesses and simulate a dependence with lower slope, and we find that the square root of the dynamic range empirically provides a good estimate for the errors. Some of the scatter about straight-line fits may also be real and due to intrinsic or viewing angle produced accelerations or changes in the complex underlying internal brightness distribution of the convolved components (Gómez et al. 1997).

Changes in the jet emission from epoch to epoch can also be examined using flux profile curves (summed flux perpen-

dicular to the jet). Figures 6a and 6b show the flux profile at each epoch plotted as a variable-width black bar, with diagonal lines indicating fits to model-fit Gaussian positions versus time. Motions of well-separated components like C4 are easy to see in these plots, while motions of inner components which often appear as extensions or "shoulders" on a declining jet are more difficult to see.

Apparent speeds of the components were measured by performing least-squares fits to the Gaussian radial positions versus time from Figures 5a and 5b, assuming radially outward motion at constant speed. The data indicate this to be a good approximation for all components except C4 (see § 4.5). For four components (C4, C5, C6, and C7) we have measured speeds at both 22 and 43 GHz. The speeds at 22 and 43 GHz are consistent (as they should be) for all of these components except C6, where the speeds at 22 and 43 GHz differ at the 2 σ level. We believe this to be due to a biasing outward of the position of C6 at 43 GHz during its short detection period at this frequency due to a blending
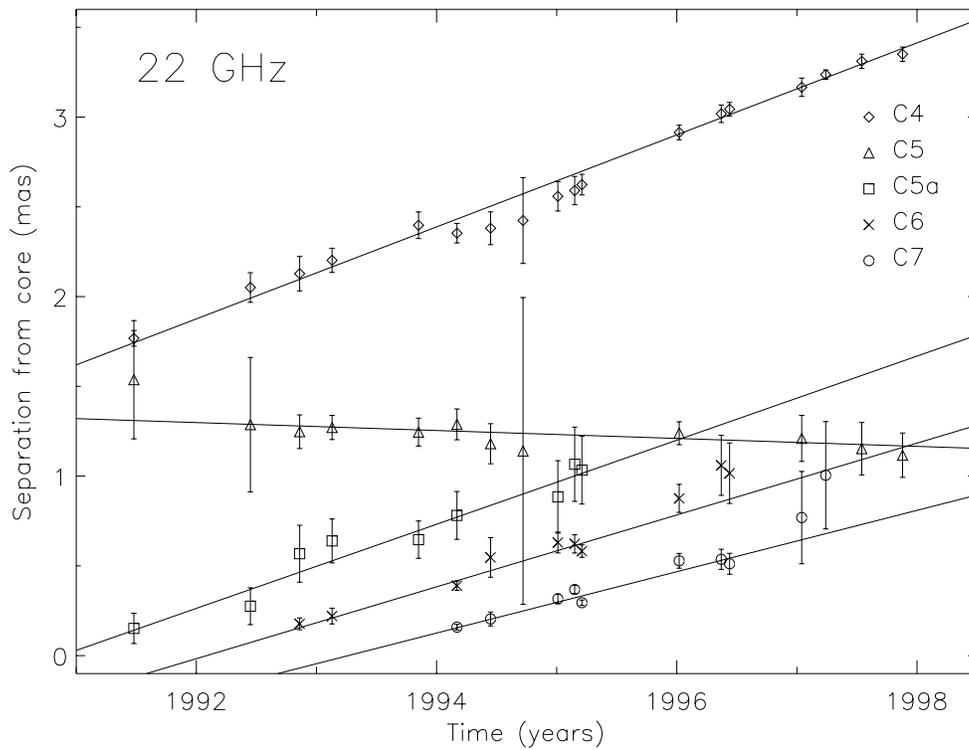
FIG. 5a
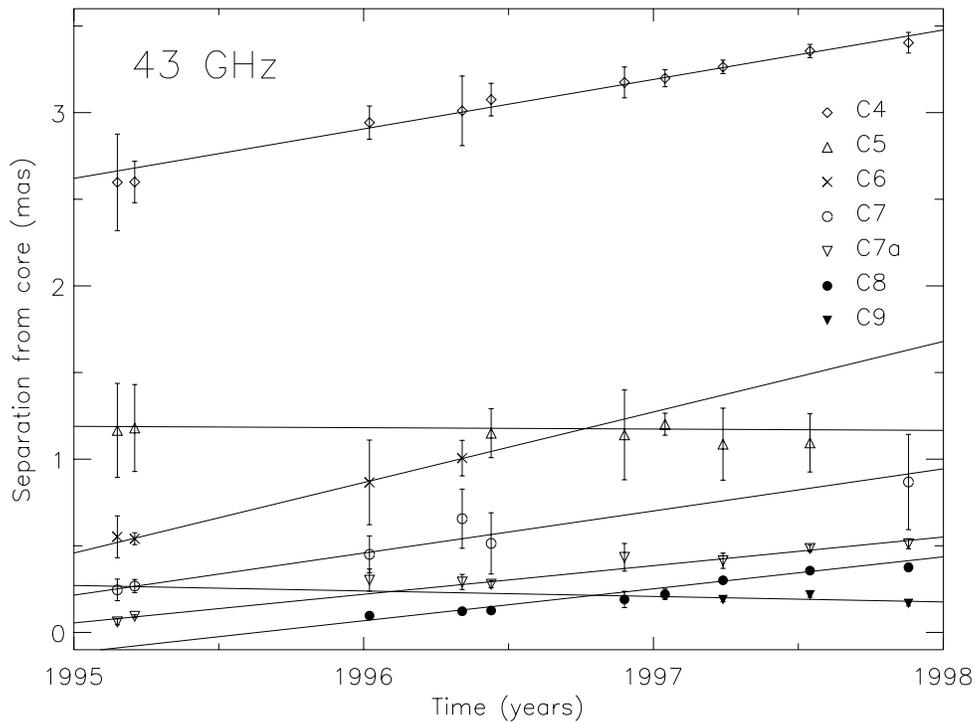
FIG. 5b

FIG. 5.—Distances from the core of model-fit Gaussians in 3C 279 as a function of time. Diamonds represent component C4, upward-pointing triangles C5, squares C5a, crosses C6, circles C7, downward-pointing triangles C7a, filled circles C8, and filled downward-pointing triangles C9. The lines shown are the best fits to motion with constant speed. (a) 22 GHz. (b) 43 GHz.

with C5, which it was then approaching. For those components detected at both frequencies, the most accurate speeds were obtained from the 22 GHz monitoring, due to its 3 times longer time baseline. The measured speeds for all components are listed in Table 4. These speeds differ signifi-

cantly from each other, with the moving components (excluding C5 and C9) becoming progressively slower from C4 to C7a, and the speed increasing slightly again with C8.

These speeds can be compared with those measured previously by other authors. 3C 279 was one of the first quasars
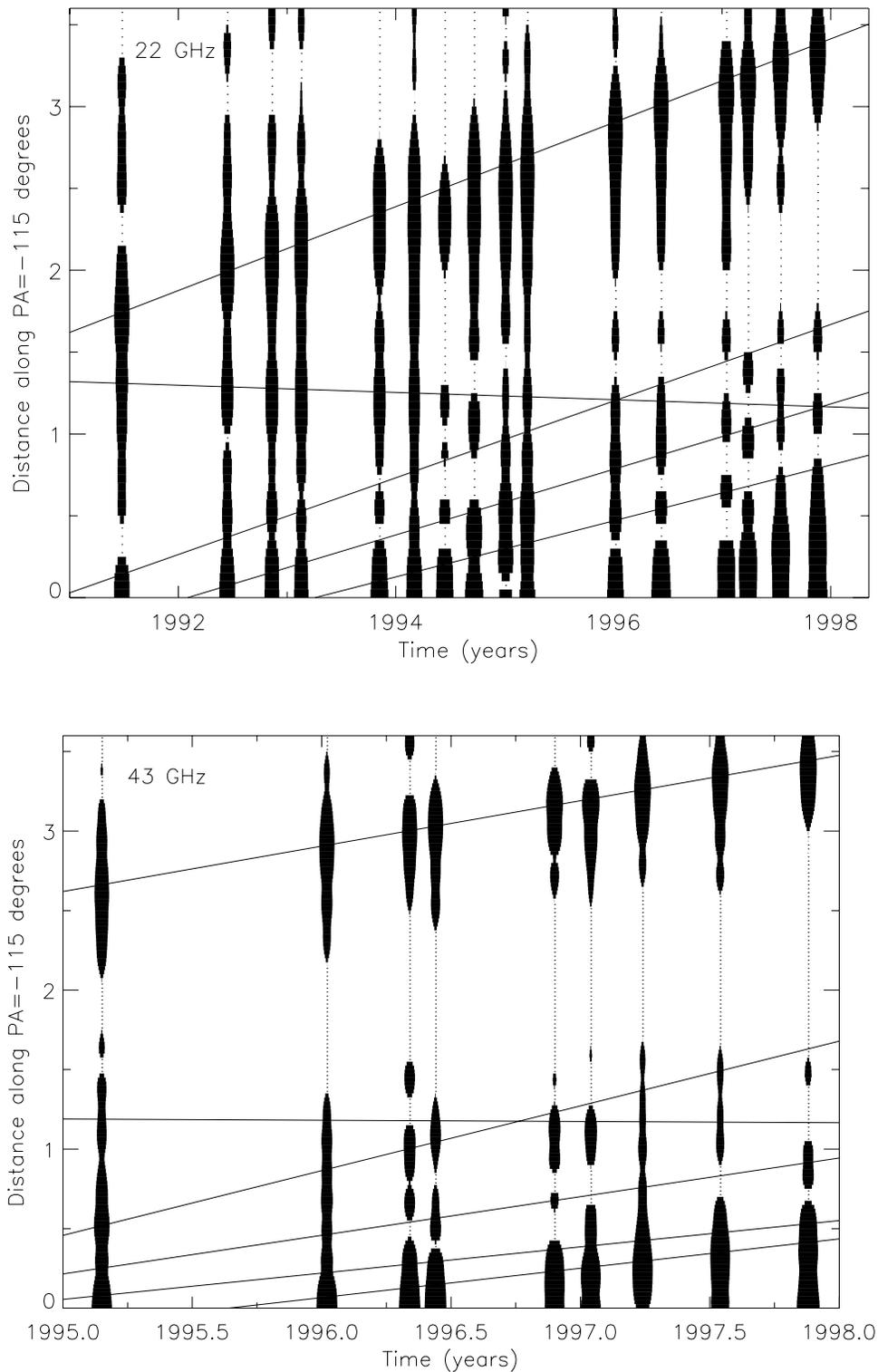
FIG. 6.—Flux profiles of the 3C 279 jet vs. time. The width of the variable-width black bar plotted for each epoch is proportional to the logarithm of the flux summed perpendicular to the jet (assumed to be at a position angle of −115°), at a distance along the jet indicated by the y-axis. A 5 Jy delta function at zero mas (representing the core) and a smoothly declining exponential jet have been subtracted from the fluxes to enhance the contrast of jet components. The solid lines show the best fits to the model-fit Gaussian positions vs. time from Figs. 5a and 5b. (a) 22 GHz. All epochs are shown with the exceptions of 1995 February 25 and 1996 May 13. (b) 43 GHz. All epochs are shown with the exception of 1995 March 19.

to have a superluminal speed measured. Older VLBI observations (Cotton et al. 1979; U89; C93) followed a series of components (C1–C3) moving along position angles of −130° to −140°. Cotton et al. (1979) reported a large

proper motion of 0.5 mas yr^{-1} (15c) during the early 1970s; their data were reexamined and their interpretation confirmed by U89. U89 and C93 observed the motions of several new superluminal components, and found that the

TABLE 4

APPEARANT SPEEDS[a]

Component	Speed (c)	Zero Separation Epoch	Frequency[b] (GHz)
C4	7.5 ± 0.2	$1984.68 \pm^{0.27}_{0.29}$	22
C5	-0.6 ± 0.5	...	22
C5a	6.8 ± 1.0	$1990.88 \pm^{0.28}_{0.39}$	22
C6	5.8 ± 0.4	$1992.09 \pm^{0.14}_{0.17}$	22
C7	5.0 ± 0.4	$1993.26 \pm^{0.13}_{0.14}$	22
C7a	4.8 ± 0.2	$1994.67 \pm^{0.04}_{0.05}$	43
C8	5.4 ± 0.2	$1995.63 \pm^{0.07}_{0.07}$	43
C9	-0.9 ± 0.8	...	43

[a] for $H_0 = 70$ km s^{-1} Mpc^{-1}, $q_0 = 0.1$.
[b] Frequency at which the speed measurement was made.

speeds of these components were only one-quarter to one-third (3c–5c) of that measured for the original superluminal component during the 1970s. Component C4 discussed in this paper was first detected in these observations of U89 and C93 at its present position angle of $-114°$. C93 determined a motion of 0.15 ± 0.01 mas yr^{-1} (4c) for C4, significantly different from the speed measured in this paper. There are a number of potential causes for this discrepancy: at the time of those observations C4 was about 1 mas from the core (near C5) in a region that is difficult to interpret, the VLBI data from the late 1980s are of inferior quality to modern VLBA data (see Appendix), and the motion of C4 is inherently complex (see § 4.5). The speed measured here for C4 agrees well with that measured in 15 GHz VLBA monitoring (K. I. Kellermann 1999, private communication). The different speeds measured for various components in our monitoring are consistent with the varying speeds observed for different components during the 1970s and 1980s and show that this variation in speed from component to component is a real property of this source.

4.3. C5 and Stationary Components

Component C5 has a fitted motion consistent with zero speed ($-0.6 \pm 0.5c$) over the 6 years from 1991 to 1997 at 22 GHz, although it does show some evolution, dimming considerably in flux over this time (see Fig. 3). Stationary jet components are a relatively common phenomenon in superluminal sources. The well-known source 4C 39.25 has long displayed a bright stationary component in addition to the core (Alberdi et al. 1999). Core-jet sources with stationary components are sufficiently common that a sizable percentage of sources originally classified as compact doubles were later found to be core-jet sources with stationary components rather than the physically distinct compact symmetric objects (Conway et al. 1994). Stationary components were also found to be a common feature of EGRET blazars in the monitoring program of Marscher et al. (2000).

Stationary components could be due to two causes: a standing shock in the jet, or a point along a curving jet where the jet crosses the line of sight. In the second case the stationary component should appear quite bright, since the jet material would have maximal Doppler boosting when passing this point. Since C5 is at times quite faint, and since there appears to be a physical change in the jet at about that point (with most superluminal components fading and disappearing at about the location of C5—possibly becoming disrupted), we favor the explanation of C5 as a standing shock in the jet. Gómez et al. (1995) find that standing

oblique shocks are created in their numerical simulations of relativistic jets by quasi-periodic recollimation shocks. A standing shock may also be created through a sudden variation in the external pressure that results in an isolated recollimation shock, and it will be an interesting future study to see if isolated stationary components correspond to a physical point in the source where the pressure would be expected to change abruptly.

The bright flux of C5 around 1991 and its subsequent decay may be due to the lingering effects of its previous encounter with C4, which passed the location of C5 in the late 1980s. If the slight inward motion measured for C5 is real, this may be due to a temporary dragging downstream of the stationary component during its interaction with C4. Gómez et al. (1997) find that both of these effects (brightening and dragging downstream of the stationary component) occur when superluminal components interact with stationary components in their relativistic jet simulations.

4.4. Component Position Angles

The kiloparsec-scale VLA jet of 3C 279 mapped by de Pater & Perley (1983) displays several components with position angles ranging from $-145°$ to $-155°$. Position angles of the older VLBI components C1–C3 measured by Cotton et al. (1979), U89, and C93 were similar: $-130°$ to $-140°$, implying slight bending between the parsec and kiloparsec scales. More recent high-dynamic range VLBA maps at lower frequencies (5 and 1.6 GHz) by Piner et al. (2000) have confirmed the larger scale VLBI jet to have components with position angles ranging from $-135°$ to $-155°$, with several small bends present between the core and the last visible component at ~ 100 mas. The current dominant feature in the smaller scale VLBI jet (C4) has a position angle of $-114°$, quite different from any of these larger scale position angles. C4 shows no signs of altering its path to follow the larger scale structure and appears to be continuing along a position angle of $-114°$. In fact, both the higher dynamic range 22 GHz images from this paper (see § 3) and the lower frequency VSOP and VLBA images from Piner et al. (2000) show steep-spectrum diffuse emission at a position angle of about $-140°$ between the core and C4, indicating that C4 has already passed the point where it would have needed to turn to follow the larger scale VLBI structure.

Figure 7 shows the position angles of C4 and the other inner jet components discussed in this paper. Since no individual component shows a significant change in position angle (with the exception of C4, where the change is smaller than the scale important for this plot), we plot the average position angle for each component. Figure 7 shows that the average position angles of jet components have changed during our monitoring. The position angles of the new components C8 and C9 are similar to that of the larger scale VLBI structure. Since these new components have only been monitored over a 1 to 2 yr time frame, it remains to be seen if their position angles will change with time to match any of the earlier components.

Abraham & Carrara (1998) attempted to explain the different apparent speeds and position angles of the older VLBI components by postulating a precessing nozzle that ejects components at varying position angles and viewing angles. While we confirm the presence of different position angles and apparent speeds for different components, our
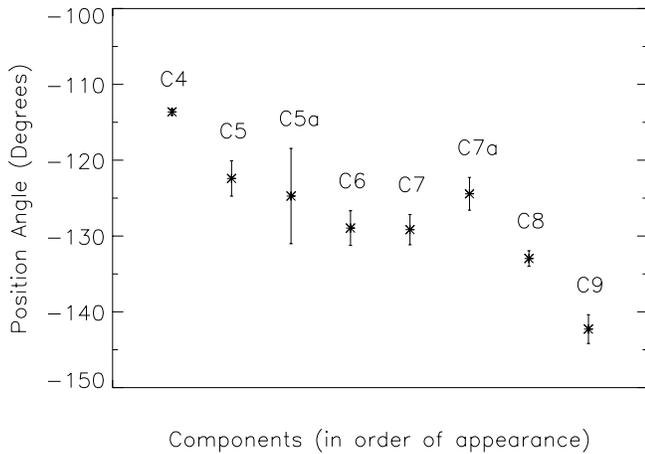
FIG. 7.—The average position angles of jet components have changed during our monitoring.

measurements do not agree with an extrapolation of their specific model to the epochs observed in this paper. Our measured apparent speeds agree reasonably well with an extrapolation of their Figure 2 (they predict a slowing of apparent speeds for ejections between 1989 and 1996), but the change in component position angles from Figure 7 does not agree with their Figure 1, and even has an opposite slope. Since the different apparent speeds and position angles are suggestive of a precessing nozzle, it may be possible for a different precession model to fit the current data; however, if component ejections really vary regularly between $-114°$ and $-142°$ on ~ 10 yr timescales as indicated by Figure 7, it is difficult to understand why the larger scale VLBI and VLA emission should be constrained to the narrow range of position angles observed.

4.5. Three-Dimensional Trajectory of Component C4

We have a large number of precise measurements of component C4 (18 at 22 GHz and 10 at 43 GHz), which enable us to track its motion in detail. We are fortunate that this component has been unusually bright and long lived and has been visible over the entire 6 years of monitoring at 22 GHz. Component C4 has followed a curved path over the years 1991 to 1997 (an indication of this can be seen in Figure 5a, where the apparent speed appears to slow around 1994). We used this curved path and measured apparent speeds to derive the complete three-dimensional trajectory of C4, using the method described by Zensus, Cohen, & Unwin (1995) for the motion of components in 3C 345 and in the earlier independent work by Wardle et al. (1994). This method is displayed graphically in Figure 8. We use the positions measured in the 22 GHz monitoring, since this has a time baseline three times longer than the 43 GHz monitoring.

We start by deriving weighted least-squares polynomial fits to $x(t)$ and $y(t)$, the measured offsets from the core in the plane of the sky at epoch t. The measured $x(t)$ and $y(t)$ values and their associated fourth-order fits are shown in Figure 8a. A straight line is a very bad fit to the measured $x(t)$ values (reduced $\chi^2 = 2.8$), and a fourth-order polynomial is the lowest order that achieves a good fit (reduced $\chi^2 = 0.71$). Zensus et al. (1995) also needed fourth-order

polynomials to fit the motion of components in 3C 345. Figure 8b shows the same measured values and fits from Figure 8a in the (x, y) plane and shows the substantial curvature in the C4 trajectory.

From the fits to $x(t)$ and $y(t)$ we derived the instantaneous apparent speed $\beta_{app}(t) \propto [\dot{x}(t)^2 + \dot{y}(t)^2]^{1/2}$, which is shown in Figure 8c. The apparent speed varies between $6c$ and $12c$ over the years 1991 to 1997. Note that Figure 8c shows the magnitude of the total velocity vector (this is more appropriate for a component following a curved trajectory), unlike Figure 5a, which shows only the radial component. These changes in β_{app} with time could be caused either by changes in the Lorentz factor Γ or the viewing angle θ (or both). Since we know the trajectory to be undergoing bends in the sky plane, a constant θ would require a special alignment of the true bends with respect to the observer, which we consider unlikely. We therefore take the other simplifying assumption (constant Γ), and assume that the changes in β_{app} with time are due to changes in θ. We assume Γ to be constant at a value slightly larger than the minimum Γ required for the maximum $\beta_{app}(t)$: $\Gamma_{min} = [\beta_{app}(t)^2 + 1]^{1/2}$, so we take $\Gamma = 13$. Under the assumption of constant Γ, we can use the observed $\beta_{app}(t)$ to calculate $\theta(t)$. Since the equation for $\theta(t)$ is quadratic, we must choose either the large or the small-angle solution, this is shown in Figure 8d. We take the small-angle solution because the large-angle solution gives large changes in the Doppler factor δ that would be seen as large changes in the flux of C4, and these are not observed. Figure 8e confirms that $\delta(t)$ shows little variation in the case of the small-angle solution.

The small-angle solution constrains C4 to viewing angles of $1°$ to $3°$. Small viewing angles such as these are typical of those expected for an EGRET blazar (see the Monte Carlo simulations of Lister 1998), and angles in this range have been successfully used to model the multiwavelength spectrum of 3C 279 by, e.g., Maraschi et al. (1992) ($3°$), Ghisellini & Madau (1996) ($4°$), and Hartman & Boettcher (1999) ($2°$). Once $\theta(t)$ is known the trajectory of the component in the (x, z) and (y, z) planes (where the z-axis is perpendicular to the plane of the sky) can be calculated. These trajectories are shown in Figure 8f (note the expanded scale along the z-axis), together with Figure 8b, they describe the complete three-dimensional motion of the component. Component C4 appears to describe approximately one oscillation of a low-pitch angle helical motion, notable especially in the (x, z) plane trajectory. Helical motion of components may be caused by hydrodynamic instabilities (Hardee 1987) or magnetohydrodynamic effects (Camenzind 1986; Camenzind & Krockenberger 1992) and has previously been observed in several sources, notably 3C 345 (Steffen et al. 1995) and BL Lac (Tateyama et al. 1998; Denn & Mutel 1999).

The bending of the trajectory of C4 is much smaller (about $4°$ total change in position angle) than the position angle differences between components shown in Figure 7. This indicates that a complete description of component motions in 3C 279 may require a superposition of small-scale wiggles—possibly due to hydrodynamic instabilities—such as those observed in the motion of C4, and a larger scale motion of the jet nozzle that causes the differences in apparent speed and position angle from component to component. This would make a complete description of motions in 3C 279 quite complex and is reminiscent of the complexity observed in 3C 345, where different components follow
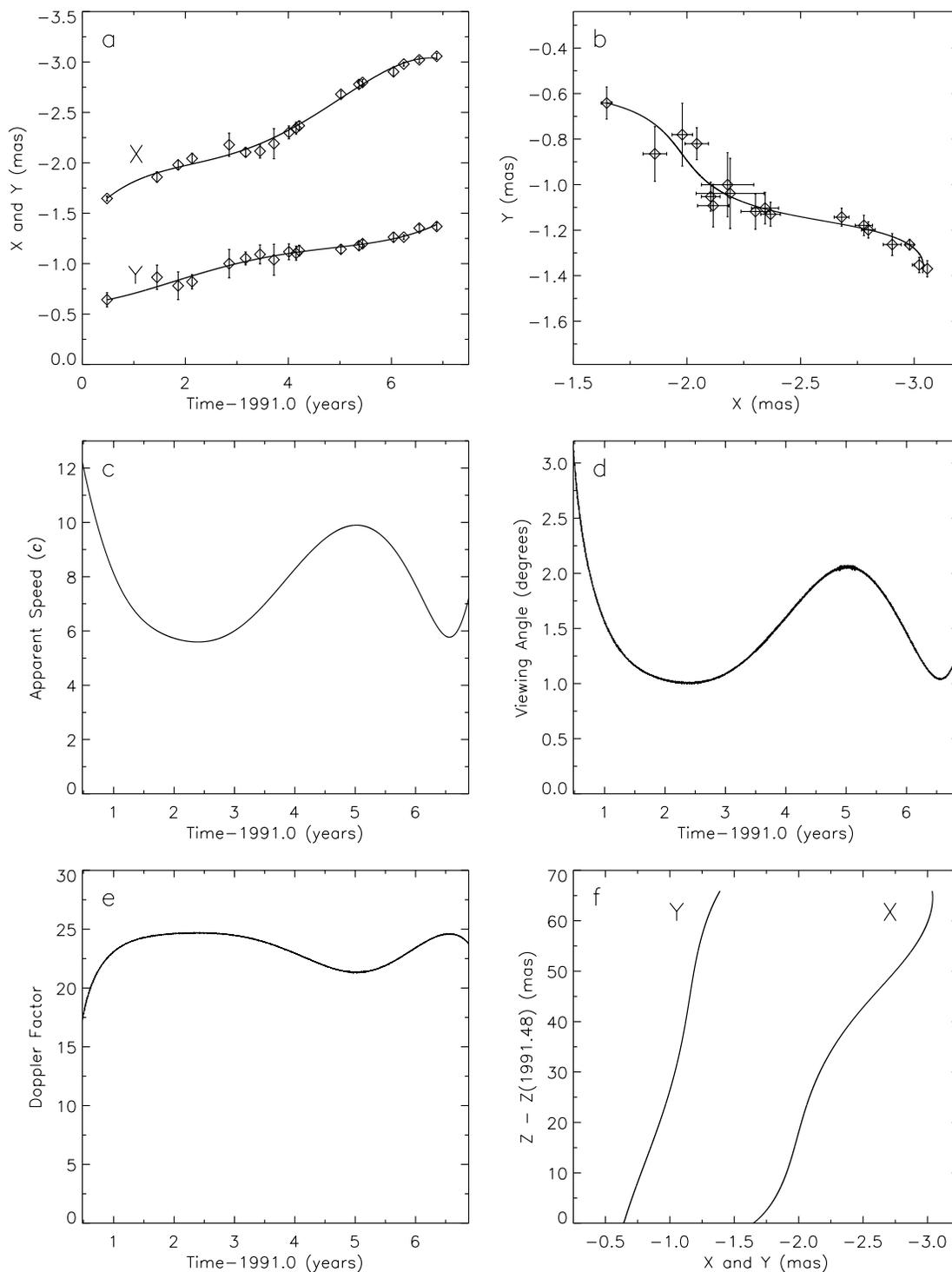
FIG. 8.—Derivation of the complete three-dimensional trajectory of component C4 at 22 GHz from 1991 to 1997. Individual panels are discussed in the text of § 4.5.

different curved paths (Zensus et al. 1995). Detailed motions of components in 3C 279 other than C4 are difficult to observe, since other components tend to fade and disappear within about 1 mas of the core. To further constrain the dynamics of the 3C 279 jet it will be necessary to continue monitoring the position of component C4 as it evolves, the bright component C8 to see if it continues past the 1 mas point (which it will reach in about 2002), and the position angles of new ejections.

4.6. Jet Opening Angle

We can measure the apparent opening angle of the 3C 279 jet using the model-fit sizes of the core and component C4. Component C4 is well resolved transverse to the jet (see Figs. 3 and 4); at many epochs an elliptical Gaussian with major axis transverse to the jet is required to model it. We used the mean core size at 22 GHz—0.07 mas, which is partially resolved, see § 5.3.1—and calculated the apparent

opening angle of C4 for each 22 GHz epoch. The median apparent full-cone opening angle is 12°. This angle can be deprojected using a typical viewing angle for C4 of 2° (an approximate upper limit since viewing angle was derived using a minimum Γ), estimated from Figure 8d, to obtain an intrinsic full-cone opening angle of 0°.4. This opening angle is quite small; for comparison, Unwin et al. (1994) derived a full-cone opening angle for 3C 345 of 5°, although this number was not well constrained. Marscher et al. (2000) mention that a number of the jets of EGRET blazars are quite broad within a few mas of the core, which suggests that they are being viewed nearly end-on. The inner jet of 3C 279, however, is relatively narrow (see Figs. 3 and 4), despite its status as an EGRET blazar, confirming an intrinsically small opening angle as derived above. Gómez et al. (1997) find small full-cone opening angles of 0°.8 in their numerical simulations of both pressure-matched and over-pressured relativistic jets.

4.7. Zero-Separation Epochs and EGRET Light Curve

In this section we examine whether any relationships can be demonstrated between the ejection epochs of the super-luminal components and γ-ray high states or "flares" observed by *CGRO* EGRET. Such a relationship could indicate that the γ-ray high states correspond to major disturbances in the energy flow of the relativistic jet. In the VLBA EGRET-blazar monitoring campaign described by Marchenko-Jorstad et al. (2000), correlations between VLBI component ejections and γ-ray flares are seen in 10 out of 19 cases of γ-ray flares for which sufficient VLBI data existed to detect such a correlation, a number far exceeding that expected by random chance.

We have extrapolated the epochs of zero separation from the core (i.e., centers coincident) of the five moving components that have emerged during the EGRET era (C5a, C6, C7, C7a, and C8) by assuming motion at the constant radial speeds given in § 4.2. The estimated epochs of zero separation are listed in Table 4. Errors on the zero-separation epochs were derived from the errors in the speeds quoted in Table 4. The component zero-separation epochs can be used to calculate the intervals between component ejections. For the five components listed above (C5a, C6, C7, C7a, and C8) the four corresponding ejection intervals are 1.21 ± 0.33, 1.17 ± 0.20, 1.41 ± 0.14, and 0.96 ± 0.08 yr. While not statistically identical, these times do suggest an ejection rate of about one component per year.

These epochs of zero separation are compared with the EGRET "light curve" in Figure 9. The EGRET fluxes have been taken from Hartman et al. (1999) (prior to 1996), and R. C. Hartman (2000, private communication) (1996 and later). Recall that EGRET viewing periods varied in length from about two weeks to seven weeks; in some periods, the full viewing period was needed to collect enough data for a single reliable detection or to form an upper limit. "Flare" indicates a high state, not that a well-defined rise and decline from a quiescent level was observed. Figure 9 clearly shows that any statistical study is hampered by the sparseness of the EGRET light curve. Inspection of Figure 9 shows that there is no overlap between any of the 1 σ ranges on component zero-separation epochs and an EGRET viewing period on 3C 279. In other words, we were never observing with EGRET when a VLBI component was being ejected.
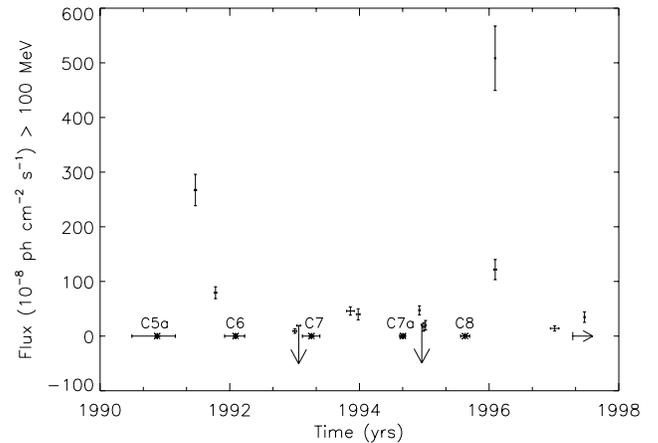
FIG. 9.—EGRET light curve compared to VLBI component zero-separation epochs. EGRET fluxes were taken from Hartman et al. (1999) and R. C. Hartman (2000, private communication). Upper limits shown are 2 σ. A residual uncertainty of 10% was used in the flux errors in addition to the statistical uncertainty as suggested by Hartman et al. (1999). Combined viewing period fluxes have been used where available and where the individual viewing period fluxes are consistent with a constant flux over the summed interval. Estimated zero-separation epochs of the VLBI components assuming constant speed are plotted as asterisks with accompanying error bars along the zero-flux line. The arrow near the right edge of the plot indicates the last epoch at which a component ejection could have been detected, assuming a component speed of 5c and detection at 0.1 mas.

There *are* components ejected close to the times of the major γ-ray "flares" in 1991 and 1996, but this may have occurred by random chance. Component C5a's zero-separation epoch is 1990.88 ± $^{0.28}_{0.39}$, prior to the γ-ray high state observation at 1991.47. Component C8's zero-separation epoch is 1995.63 ± $^{0.07}_{0.07}$, prior to the γ-ray high state observation at 1996.09. A correlation cannot be demonstrated statistically because the EGRET data are too sparsely sampled; however, "Absence of evidence is not evidence of absence." The next-generation γ-ray satellite, *GLAST*, will be much more suited to statistical studies.

5. FLUX AND SPECTRAL EVOLUTION OF THE CORE AND JET

5.1. Radio Light Curves

In this section we discuss the relation between the evolution in brightness of individual VLBI components and that of the total source flux. The motivation for this approach is to take advantage of the very long history of flux monitoring of 3C 279. Regular monitoring at centimeter wavelengths was begun by the Michigan group in 1965 (Aller et al. 1985), and the source is now monitored at intervals of a few days to frequencies as high as 87 GHz.

It is clear from the Michigan radio light curves at 4.8, 8.0 and 14.5 GHz that the character of the flux curves changed in 1990. Prior to 1990, individual flux outbursts were well separated, by intervals of up to 5 yr. The 1981–1985 burst was well fitted by a shock model in which the low-frequency evolution lagged the higher frequencies (Hughes, Aller, & Aller 1991). Until 1990, the spectrum between 8 and 14.5 GHz remained essentially flat ($\alpha \sim 0$), but since then, the spectrum has been strongly inverted. Even more striking, the characteristic timescale for flux outbursts has decreased to less than a year, with detectable changes on scales of a week or less.

This increase in complexity of the total flux light curves does not correspond to any increase in the complexity of the VLBI images. The simplest explanation is that the bulk of the flux variation occurs in the almost-unresolved core. Figure 10a shows the flux density evolution of the core and jet components from model fitting at 22 GHz. Also shown are the 22 GHz total flux density monitoring data from Metsähovi. Figure 10b shows the same data over a smaller range in flux so that the variability of the jet components can be seen. Similarly, Figure 10c shows the 43 GHz core and jet component fluxes and 37 GHz Metsähovi data, and Figure 10d shows the same data over a smaller range in flux. We estimate the amplitude calibration of these VLBI fluxes to be accurate at about the 10% level.

The VLBI data are clearly undersampled, even though 3C 279 is one of the best-observed AGNs with VLBI. However, the obvious correlation between the VLBI core and total flux light curves shows that flux variations in the core are largely responsible for the total flux variability. The logarithmic contours on the image series (Figs. 1–4) tend to suppress these changes, with the result that the image evolution appears to be largely uncorrelated. A consequence of

this is that relating flux variations in the more distant components to the total flux will be very difficult, because they are masked by the much stronger core variations. This behavior of 3C 279 (where the total flux variability is dominated by the VLBI core and the jet components are much weaker than the core) is quite different from its behavior in the early 1980s, when the total flux density variations were dominated by component C3 (U89), and from that of 3C 345, where the total flux variability has been linked to new jet components which have all surpassed the core in brightness (Valtaoja et al. 1999).

The flux history of the VLBI components generally shows a fading with time, with component lifetimes of roughly 3 yr. Exceptions to this are components C4, which has maintained an approximately constant flux over the 6 yr monitoring period and shows no signs of fading, and C5, which at first faded but then maintained an approximately constant flux. Components C6 and C7a both fade at first but then show secondary increases in flux; such an increase could be due to a changing Doppler factor along a slightly curving path. 3C 279 ejected an exceptionally bright component (C8) in late 1995. This component was first detected
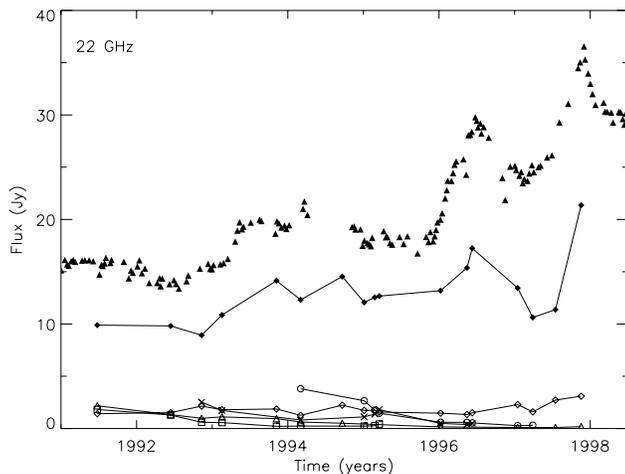
FIG. 10a
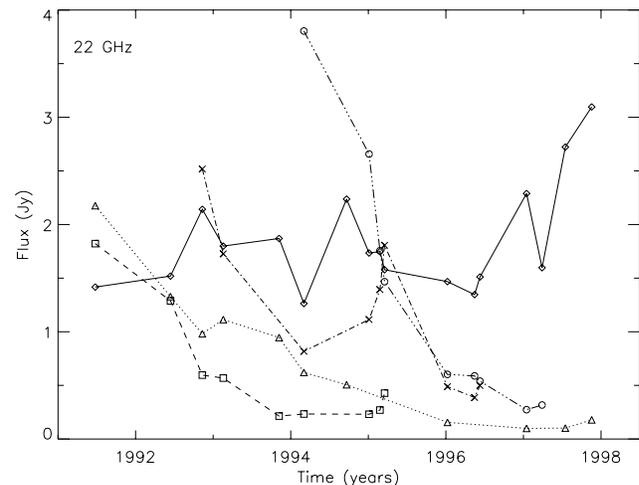
FIG. 10b
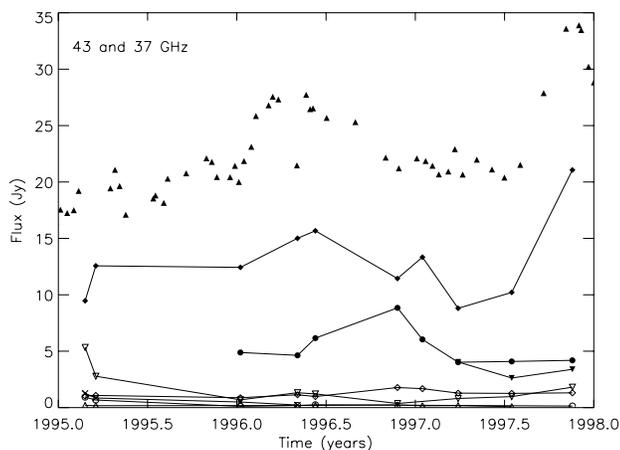
FIG. 10c
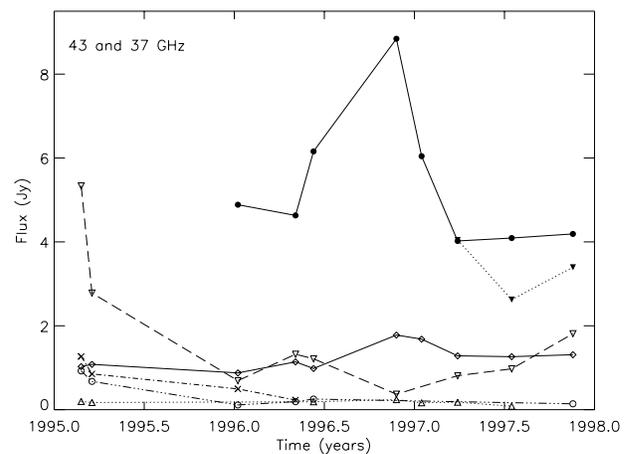
FIG. 10d

FIG. 10.—VLBI and total flux light curves of 3C 279. The filled upward-pointing triangles in panels (a) and (c) represent total flux density monitoring data from Metsähovi at 22 and 37 GHz, respectively. Other symbols represent VLBI model-fit fluxes: filled diamonds the core, open diamonds C4, upward-pointing triangles C5, squares C5a, crosses C6, circles C7, downward-pointing triangles C7a, filled circles C8, and filled downward-pointing triangles C9. The poor sensitivity observation on 1994 June 12 is not included. (a) 22 GHz. (b) 22 GHz with an expanded flux scale to show variability of jet components. (c) 43 GHz. (d) 43 GHz with an expanded flux scale to show variability of jet components.

with a flux density of 5 Jy, it then rose in flux until it reached 9 Jy (making it the single exception to our previous statement that the jet components in 3C 279 were generally much weaker than the core), it later faded to a flux density of 4 Jy at the end of our monitoring in 1997.

5.2. Radio Spectrum

The 22 and 43 GHz images and model fits can be used to calculate two-point spectral indices. Considering first the model-fit Gaussian fluxes, we calculate mean values for the spectral index of the core and C4 to be -0.16 and -0.70, respectively, for $S \propto v^{+\alpha}$. Variations in spectral index from epoch to epoch are difficult to distinguish from flux errors due to calibration or model fitting, making it difficult to draw conclusions about spectral index variations with time from these observations. Similarly, it is difficult to quantify the spectral index of the inner jet components from the model fits, since the inner jet is a complex area with multiple components and subject to component blending at 22 GHz.

The approximately flat index for the core indicates a synchrotron turnover frequency between 22 and 43 GHz. This is consistent with the results of Grandi et al. (1996), who concluded the turnover frequency lay between 37 and 90 GHz based on total flux density monitoring from 1992 December to 1993 January. The turnover frequency of the core is variable; U89 found a turnover frequency around 11 GHz based on their three-frequency VLBI observations from 1983. The steep spectral index of C4 indicates that this component is optically thin above 22 GHz. Piner et al. (2000) found a spectral index for C4 of $+0.25$ between 1.6 and 5 GHz, placing the turnover frequency for C4 between 5 and 22 GHz.

5.3. Radio Core Brightness Temperatures

5.3.1. Brightness Temperature Estimates

Brightness temperature values can be used to constrain both Doppler beaming factors and physical processes occurring in a source. The maximum brightness temperature of a circular Gaussian[10] is given by

$$T_B = 1.22 \times 10^{12} \frac{S(1+z)}{a^2 v^2} \text{ K} , \qquad (1)$$

where S is the flux density of the Gaussian in Janskys, a is the FWHM of the Gaussian in mas, v is the observation frequency in GHz, and z is the redshift. A fact that is often neglected is that the minimum measurable size depends on the signal-to-noise of the observations, because a smaller slope in the amplitude versus (u, v) distance plane can be measured when the error bars on the visibilities are smaller. An expression for the minimum measurable size in the visibility plane is given by Lovell et al. (2000) to be

$$a < \frac{2.4\sqrt{N/S}}{U} \text{ mas} , \qquad (2)$$

where N is the integrated rms noise of the observations in Janskys and U is the maximum baseline length in units of 100 Mλ. Expressed in terms of a uniformly weighted beam size, $\theta_{\text{beam}} \approx 1.34 \times 10^8 \lambda/d$ mas, this is $a < 1.8(N/S)^{1/2}\theta_{\text{beam}}$ mas. Inserting equation (2) into equation (1), the maximum

---

[10] A Gaussian brightness distribution is the only brightness distribution fully supported in DIFMAP.

measurable brightness temperature is

$$T_B = 235 \frac{S^2 D^2 (1+z)}{N} \text{ K} , \qquad (3)$$

where D is the maximum baseline length in kilometers. The maximum measurable brightness temperature depends on the source flux squared, because of the dependence of minimum measurable size on the SNR. For an observation of 3C 279 with the VLBA at 22 GHz with $S \sim 10$ Jy, $N \sim 10$ mJy, and $D \approx 8600$ km, the minimum measurable size is about 1/20 of a beam, and the maximum measurable brightness temperature is over 10^{14} K. The commonly quoted limit of $\sim 10^{12}$ K for Earth-size baselines is based on a canonical 1 Jy source and a minimum measurable size of about $\frac{1}{3}$ of a beam.

Brightness temperatures for the core of 3C 279 from our 22 and 43 GHz model fits are listed in Table 5. Upper and lower limits to the brightness temperature at each epoch are also given; these upper and lower limits were calculated using the Difwrap program (Lovell 2000) as described by Piner et al. (2000). In some cases, a model-fit brightness temperature in excess of that given by equation (3) is obtained, these values are indistinguishable from an infinite brightness temperature, i.e., the component cannot be resolved with the given data. In these cases, the lower limit to the brightness temperature is a more meaningful number than the best-fit value.

Note that allowable ranges for the core size and flux were derived for visibilities self-calibrated to the CLEAN images shown in this paper. We performed several tests to assess how self-calibrating to the variable Gaussian models could affect the allowed ranges of core size and core flux. Repeated self-calibration and model fitting to the Gaussian models from Table 3 with the core size or flux displaced from the best-fit value allowed larger ranges of these parameters to fit the visibilities, but Gaussian models obtained in this fashion no longer accurately represented the corresponding CLEAN image. When only a single Gaussian at the core location was used—with the rest of the source structure represented by fixed CLEAN components to retain the constraints provided by the hybrid mapping procedure—then repeated self-calibration and model fitting to this Gaussian, with the size or flux displaced from the best-fit value, produced about the same range of allowable brightness temperatures as those given in Table 5.

The brightness temperatures at 22 GHz in Table 5 can be divided into two time ranges: from 1991 through 1995 the upper and lower limits are consistent with a constant brightness temperature between 6.3 and 8.0×10^{12} K; after 1995 the upper and lower limits are consistent with a constant brightness temperature between 18.4 and 21.3×10^{12} K, indicating an increase in the brightness temperature sometime during 1995. At 43 GHz all brightness temperature limits are consistent with a constant brightness temperature between 7.6 and 8.9×10^{12} K, with the exception of the 1997 March 29 and 1997 July 16 epochs which have lower brightness temperatures. For comparison, Piner et al. (2000) found a maximum brightness temperature lower limit of 5×10^{12} K for 3C 279 from VSOP observations at 1.6 GHz. For observations at the same frequencies, VSOP should be able to measure brightness temperatures about a factor of 2 higher than the VLBA (from inserting relevant baseline lengths and sensitivities

TABLE 5
3C 279 Radio Core Gaussian Brightness Temperatures

	22 GHz			43 GHz		
		Min.[a]	Max.[b]		Min.[a]	Max.[b]
Epoch	T_B (10^{12} K)	T_B (10^{12} K)	T_B (10^{12} K)	T_B (10^{12} K)	T_B (10^{12} K)	T_B (10^{12} K)
1991 Jun 24	3.8	2.3	20.8	...	...	...
1992 Jun 14	3.4	2.0	8.1	...	...	...
1992 Nov 10	51.5	5.4	∞	...	...	...
1993 Feb 17	5.5	3.0	11.5	...	...	...
1993 Nov 8	11.6	6.3	∞	...	...	...
1994 Mar 2	6.8	4.6	10.6	...	...	...
1994 Jun 12	6.4	3.8	12.5	...	...	...
1994 Sep 21	5.6	3.5	8.0	...	...	...
1995 Jan 4	9.1	4.8	15.2	...	...	...
1995 Feb 25	6.3	3.0	18.4	∞	4.7	∞
1995 Mar 19	7.1	4.9	11.0	12.6	7.6	20.0
1996 Jan 7	13.3	8.9	27.1	7.5	5.0	9.4
1996 May 4	...	...	...	19.0	6.6	∞
1996 May 13	15.5	12.1	25.2	...	...	...
1996 Jun 9	38.2	18.4	116	7.4	5.6	8.9
1996 Nov 24	...	...	...	5.4	3.9	11.0
1997 Jan 15	∞	11.0	∞	18.1	7.0	∞
1997 Mar 29	∞	11.7	∞	2.9	2.2	3.9
1997 Jul 16	21.9	8.0	∞	4.1	2.5	5.7
1997 Nov 16	13.4	7.4	21.3	9.1	6.7	13.0

[a] Lower limit to the brightness temperature calculated using the Difwrap program.

[b] Upper limit to the brightness temperature calculated using the Difwrap program. In all cases where a numerical value is quoted rather than infinity, this value is less than the maximum measurable brightness temperature given by eq. (3).

into eq. [3]); however, the inverted spectrum of 3C 279 means that a higher brightness temperature can be measured with the VLBA near the turnover frequency than at lower frequencies with VSOP.

The core of 3C 279 is partially resolved in the majority of these observations. The high brightness temperatures estimated at 22 GHz of $\sim 2 \times 10^{13}$ K are considerably less than the maximum measurable brightness temperature derived above for these observations of over 10^{14} K. The estimated sizes are also larger than the minimum measurable sizes given by equation (2), and a considerable worsening of the fit is found at many epochs for a zero-size Gaussian. Average core sizes are 0.07 mas at 22 GHz and 0.045 mas at 43 GHz. These sizes are consistent with an inhomogeneous jet model such as the Königl model (Königl 1981), where the "core" at different frequencies is viewed further down an expanding jet, with the minimum size occurring at the turnover frequency.

5.3.2. Brightness Temperature Implications

The estimated brightness temperature of $\sim 2 \times 10^{13}$ K after 1995 at 22 GHz is among the highest direct estimates of brightness temperature (using a size rather than a variability timescale). Similar high brightness temperatures of a few times 10^{12} to 10^{13} K have been recorded in observations of other sources by the VSOP mission (Bower & Backer 1998; Lovell et al. 2000; Preston et al. 2000; Shen et al. 1999). Observed brightness temperatures are increased by the Doppler factor, and there are several mechanisms that may act to limit the rest-frame brightness temperature of a synchrotron source: rapid energy loss by inverse Compton emission that limits the brightness temperature to $\sim 5 \times 10^{11}$–1×10^{12} K (Kellermann & Pauliny-Toth

1969), induced Compton scattering that limits the brightness temperature to $\sim 2 \times 10^{11}$ K (Sincell & Krolik 1994), and equipartition of energy between particles and fields that limits the brightness temperature to $\sim 5 \times 10^{10}$–1×10^{11} K (Readhead 1994). Since these limiting brightness temperatures were all derived for homogeneous optically thick spheres, our Gaussian brightness temperatures should be converted to homogeneous sphere brightness temperatures for comparison, by multiplying by the appropriate conversion factor of 0.56, which is valid for partially resolved components (Pearson 1995; Hirabayashi et al. 1998, in particular the correction in the erratum to this paper). The highest brightness temperatures at 22 GHz are then $\sim 1 \times 10^{13}$ K, implying Doppler factors of 10–20, 50, or 140, respectively for the three limiting cases discussed above (the actual equipartition brightness temperature for 3C 279 from eq. [4a] of Readhead 1994 is $\sim 7 \times 10^{10}$ K).

Monte Carlo simulations of the EGRET blazar sample by Lister (1998) predict a Doppler factor distribution with a tail extending up to $\delta \approx 50$. However, these simulations were based on a maximum observed jet speed of 15 h^{-1} c. Since recent results on the apparent speeds in EGRET blazars (Marscher et al. 2000) show speeds up to ≈ 30 h^{-1} c ($\approx 45c$ for $h = 0.65$), revised simulations should show Doppler factors extending up to $\delta \approx 100$. Such high Doppler factor sources would be intrinsically rare as evidenced by the absence of such high speeds in radio-selected samples (Kellermann et al. 2000), and would only be present in samples that have a stronger orientation bias as has been suggested for the EGRET sample (Marscher et al. 2000). When combined with the apparent jet speeds in 3C 279 (§ 4.2), a Doppler factor $\delta \sim 100$ implies an extremely small viewing angle and an extremely small opening angle. If the

Doppler factor is this high in the radio core then it is likely reduced by a slight bend of the radio jet away from the line of sight by the time VLBI scales have been reached. Note that the Doppler factor shown for C4 in Figure 8e (§ 4.5) is not a measurement, since we assumed a constant Γ close to the minimum value allowed by the observed speed of C4. A higher Γ raises δ in Figure 8e, decreases viewing angle in Figure 8d, and stretches the vertical scale in Figure 8f.

If an independent measurement of another function of the Doppler factor exists then the rest-frame brightness temperature and Doppler factor can be found. Such a quantity is the variability brightness temperature (Lähteenmäki et al. 1999). The variability brightness temperature measured for 3C 279 is 2.3×10^{14} K (Lähteenmäki & Valtaoja 1999) and was measured at 37 GHz for a flare peaking at 1995.2 (A. Lähteenmäki 1999, private communication). Comparing this to the lower limit to the 43 GHz VLBI brightness temperature at this epoch (4.3×10^{12} K for a homogeneous sphere), we obtain a rest-frame brightness temperature of 6×10^{11} K and a Doppler factor of 7.4 using equations from Lähteenmäki et al. (1999). This implies that the jet of 3C 279 is particle-dominated by many orders of magnitude, and the brightness temperature is limited by inverse Compton effects. Slysh (1992) argues that such a high rest-frame brightness temperature can be maintained on a time-scale of years following the injection of electrons of sufficiently high energy or can be maintained indefinitely with continuous in situ electron acceleration. In this case, the Doppler factor for the 3C 279 core is at the low end of the distribution expected for EGRET sources (Lister 1998), and the jet must bend toward the line of sight as it moves from the core to C4, since the Doppler factor shown for C4 in Figure 8e is a lower limit for this component.

The Doppler factors and rest-frame brightness temperatures suggested by equipartition and by the variability brightness temperature are discrepant for 3C 279. This suggests that one of the following situations is true:

1. 3C 279 is approximately in equipartition and has an extremely high Doppler factor ($\delta \sim 100$) in the tail end of the distribution expected for EGRET blazars from the simulations of Lister (1998). This means the variability brightness temperature measured for 3C 279 is a lower limit and the actual variability brightness temperature is much larger (calculated rest-frame brightness temperature goes down and δ goes up as the variability brightness temperature increases for a given VLBI brightness temperature, see eqs. [6]–[8] of Lähteenmäki et al. 1999). This could only occur if extremely rapid variations in the 3C 279 light curve had been missed.

2. The measured variability brightness temperature is correct and 3C 279 has a strongly particle-dominated parsec-scale jet where the rest-frame brightness temperature is high and limited by inverse Compton effects. In this case the Doppler factor for the 3C 279 core would be at the low end of the distribution expected for EGRET sources from the simulations of Lister (1998).

6. CONCLUSIONS

We have presented the results from our intensive high-frequency VLBI monitoring of 3C 279 during the years 1991 to 1997. Three major results of this study are the following:

1. Apparent speeds measured for six superluminal components range from $4.8c$ to $7.5c$.

2. Comparison of VLBI and single-dish light curves from Metsähovi show that variations in the total flux density light curves can mainly be accounted for by changes in the VLBI core flux density, not the jet. This contrasts both with 3C 279's behavior in the early 1980s (U89) and with that of 3C 345 (Valtaoja et al. 1999), because in both of these cases total flux density increases were linked to the youngest jet component.

3. The VLBI core is partially resolved and has a size of ~ 0.07 mas at 22 GHz and ~ 0.045 mas at 43 GHz. The uniform-sphere brightness temperature at 22 GHz is $\sim 1 \times 10^{13}$ K after 1995, which is one of the highest direct estimates of a brightness temperature. If the variability brightness temperature measured for 3C 279 by Lähteenmäki & Valtaoja (1999) is an actual value and not a lower limit, then the rest-frame brightness temperature of 3C 279 is quite high and limited by inverse Compton effects rather than equipartition.

Other conclusions are as follows:

4. Component C4 has been very long lived and was detected at all epochs. C4 followed a curved path, and we were able to reconstruct its three-dimensional trajectory by fitting polynomials to its position versus time. The reconstructed trajectory is suggestive of low pitch angle helical motion, and constrains the path of C4 to lie within $\sim 2°$ of the line of sight.

5. There is a stationary component at ~ 1 mas that fades and may move slightly inward during the course of our observations. This behavior could be due to a previous interaction with C4, and resembles the interactions between superluminal and stationary components seen in simulations by Gómez et al. (1997).

6. Components in the inner jet were relatively short lived and faded by the time they reached ~ 1 mas from the core.

7. The VLBI components have different speeds and position angles from each other, but these differences do not match the differences predicted by the precession model of Abraham & Carrara (1998). The position angles also differ from that of the larger scale structure. The longer lived component C4 shows no signs of altering its position angle to match that of the larger scale structure.

8. The intrinsic jet opening angle is constrained to be smaller than about half a degree by the size and reconstructed trajectory of C4.

9. Although VLBI components were born about six months prior to each of the two observed γ-ray high states, the sparseness of the γ-ray data prevents a statistical analysis of possible correlations.

10. The VLBI core spectrum indicates the core turnover frequency is between 22 and 43 GHz. Comparison of C4's flux to that at lower frequencies suggests a turnover frequency for this component between 5 and 22 GHz.

Completion of this large number of epochs moves 3C 279 into the category of sources (such as 3C 345) for which large VLBI databases exist for detailed studies of jet properties. We suggest readers view the animations made from these observations at ftp://sgra.jpl.nasa.gov/pub/users/glenn/3c279_22ghz.mpeg and 3c279_43ghz.mpeg to fully appreciate the complexity of this source as revealed by

1980s 22 GHz VLBI Observations

Epoch	Experiment Name	VLBA Antennas	Other Antennas[a]	Bandwidth (MHz)	Obs. Time (minutes)	Frequencies (GHz)	Polarization
1984 Oct 2	...	...	Eb, Gb, Hs, Mp, On, Ov, Y1	2	454	22	LCP
1985 Oct 1	U15G	...	Eb, Gb, Hs, Mp, On, Ov, Y1	2	384	22	LCP
1987 Jun 4	Z13G-AH	...	Eb, Gb, Hs, Mc, On, Ov, Y1	2	569	22	LCP
1988 Feb 28......	U17G	...	Eb, Gb, Hs, On, Ov	2	616	22	LCP

[a] Antenna locations and sizes are as follows: (Eb) Effelsberg, Germany, 100 m; (Gb) Green Bank, WV, 43 m; (Hs) Haystack, MA, 37 m; (Mc) Medicina, Italy, 32 m; (Mp) Maryland Point, MD, 26 m; (On) Onsala, Sweden, 20 m; (Ov) Owens Valley, CA, 40 m; (Y1) one antenna of the VLA, Socorro, NM, 25 m.
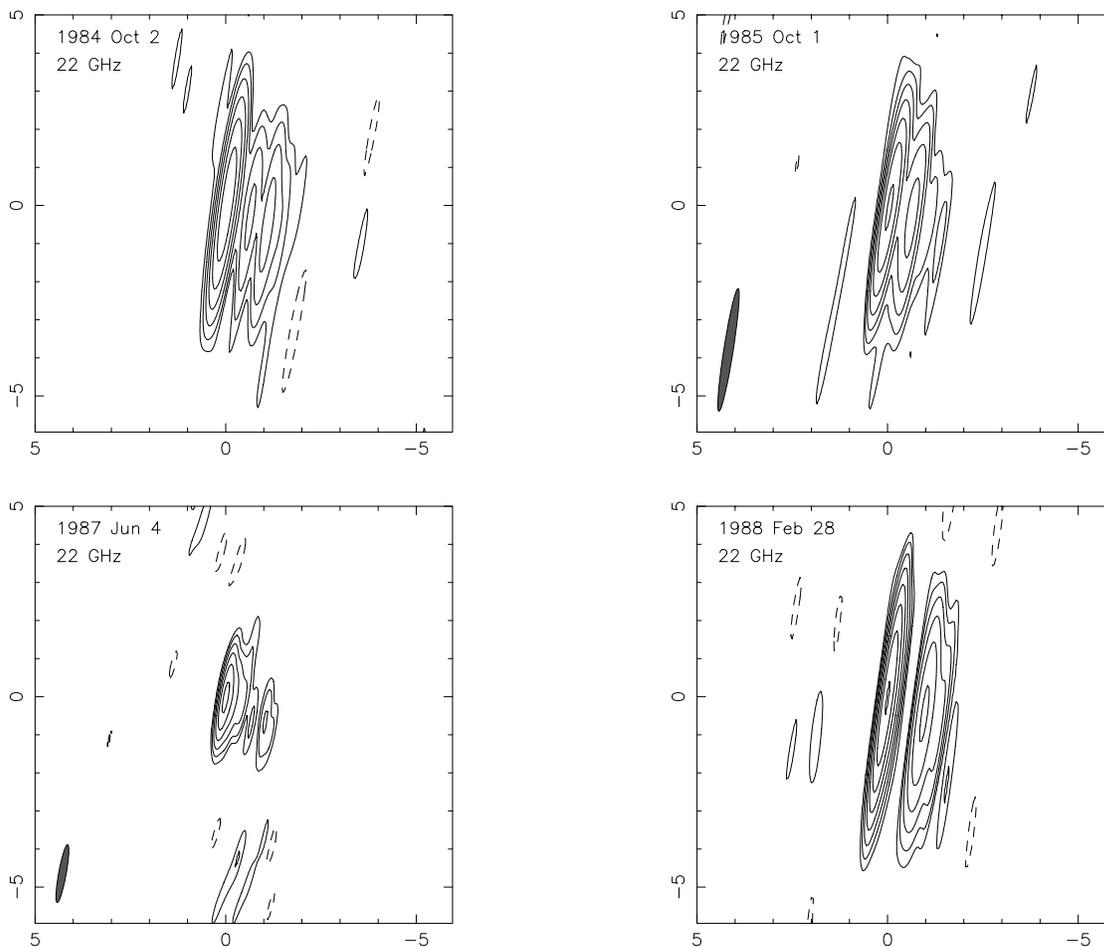
FIG. 11.—22 GHz uniformly weighted images of 3C 279 from the four epochs listed in Table A1. The axes are labeled in milliarcseconds. Parameters of the images are given in Table A2.

TABLE A2

1980s 22 GHz Image Parameters

Epoch	Frequency (GHz)	Beam[a]	Total Flux[b] (Jy)	CLEAN Flux (Jy)	Peak Flux (Jy beam^{-1})	Lowest Contour[c] (mJy beam^{-1})	Contours[d] (Multiples of Lowest Contour)
1984 Oct 2	22	3.35, 0.27, −8.1	9.7	9.8	5.8	103	$1...2^5$
1985 Oct 1	22	3.26, 0.24, −8.9	9.2	9.1	5.1	71.9	$1...2^6$
1987 Jun 4	22	1.54, 0.20, −10.3	10.4	10.1	6.0	149	$1...2^5$
1988 Feb 28......	22	3.47, 0.22, −8.1	11.9	11.2	6.5	48.6	$1...2^7$

[a] Numbers given for the beam are the FWHMs of the major and minor axes in mas, and the position angle of the major axis in degrees. The beam has been synthesized using uniform weighting.
[b] Single-dish flux from Metsähovi at 22 or 37 GHz.
[c] The lowest contour is set to be three times the rms noise in the full image.
[d] Contour levels are represented by the geometric series $1...2^n$, e.g., for $n = 5$ the contour levels would be $3 \pm 1, 2, 4, 8, 16, 32$.

multiepoch monitoring. Possible studies using this large amount of data could include application of specific hydrodynamic instability or magnetohydrodynamic models to the motion of C4, or application of precession models to the differing speeds and position angles of components using much more data than was used for the precession model of Abraham & Carrara (1998). Future data reduction will include performing the polarization analysis of the polarization-sensitive observations listed in Table 1 and analyzing all unreduced lower frequency VLBI observations. Together with data from this paper, X-ray data, and γ-ray data, this should allow us to test inverse Compton models against the multiwavelength spectrum (Piner et al. 2001, in preparation). It will be important to continue monitoring 3C 279 with the VLBA throughout the years between the EGRET and *GLAST* missions, so that a deeper understanding of this canonical γ-ray blazar can be obtained before the launch of the next γ-ray mission.

APPENDIX

22 GHz VLBI OBSERVATIONS FROM THE 1980s

In this Appendix we present early 22 GHz VLBI observations from our monitoring program. These data have been previously published by U89 and C93, but we have reimaged the data using the interactive imaging and editing capabilities of DIFMAP, which has resulted in significant improvements. These early VLBI observations are listed in Table A1, which is analogous to Table 1 in the main text. The remade images are shown in Figure 11; these should now be used in place of the corresponding images from U89 and C93. The parameters of these images are listed in Table A2, which is analogous to Table 2 in the main text. The low SNR of these observations and the high ellipticity of the beams causes model fitting to produce ambiguous results. This, together with the 3 yr gap between the 1988 and 1991 epochs, means that results from these images cannot be consistently connected to the image series presented in the main text.

REFERENCES

Abraham, Z., & Carrara, E. A. 1998, ApJ, 496, 172
Akujor, C. E., Lüdke, E., Browne, I. W. A., Leahy, J. P., Garrington, S. T., Jackson, N., & Thomasson, P. 1994, A&AS, 105, 247
Alberdi, A., Gómez, J. L., Marcaide, J. M., Pérez-Torres, M. A., & Marscher, A. P. 1999, New Astron. Rev., 43, 731
Aller, H. D., Aller, M. F., Latimer, G. E., & Hodge, P. E. 1985, ApJS, 59, 513
Bower, G. C., & Backer, D. C. 1998, ApJ, 507, L117
Carrara, E. A., Abraham, Z., Unwin, S. C., & Zensus, J. A. 1993, A&A, 279, 83 (C93)
Cawthorne, T. V., & Gabuzda, D. C. 1996, MNRAS, 278, 861
Camenzind, M. 1986, A&A, 156, 136
Camenzind, M., & Krockenberger, M. 1992, A&A, 255, 59
Cohen, M. H., Cannon, W., Purcell, G. H., Shaffer, D. B., Broderick, J. J., Kellermann, K. I., & Jauncey, D. L. 1971, ApJ, 170, 207
Condon, J. J. 1997, PASP, 109, 166
Conway, J. E., Myers, S. T., Pearson, T. J., Readhead, A. C. S., Unwin, S. C., & Xu, W. 1994, ApJ, 425, 568
Cotton, W. D., et al. 1979, ApJ, 229, L115
Denn, G. R., & Mutel, R. L. 1999, BAAS, 194, 5032
de Pater, I., & Perley, R. A. 1983, ApJ, 273, 64
Fomalont, E. B. 1985, in Synthesis Imaging, ed. R. A. Perley, F. R. Schwab, & A. H. Bridle (Green Bank: NRAO), 215
Ghisellini, G., & Madau, P. 1996, MNRAS, 280, 67
Gómez, J. L., Martí, J. M., Marscher, A. P., Ibáñez, J. M., & Alberdi, A. 1997, ApJ, 482, L33
Gómez, J. L., Martí, J. M., Marscher, A. P., Ibáñez, J. M., & Marcaide, J. M. 1995, ApJ, 449, L19
Grandi, P., et al. 1996, ApJ, 459, 73
Hardee, P. E. 1987, ApJ, 318, 78
Hartman, R. C., et al. 1999, ApJS, 123, 79
Hartman, R. C., & Boettcher, M. 1999, BAAS, 195, 1503
Hirabayashi, H., et al. 1998, Science, 281, 1825
Homan, D. C., & Wardle, J. F. C. 1999, AJ, 118, 1942
Hughes, P. A., Aller, H. D., & Aller, M. F. 1991, ApJ, 374, 57
Kellermann, K. I., & Pauliny-Toth, I. I. K. 1969, ApJ, 155, L71
Kellermann, K. I., Vermeulen, R. C., Zensus, J. A., & Cohen, M. C. 2000, in Astrophysical Phenomena Revealed by Space VLBI, ed. H. Hirabayashi, P. G. Edwards, & D. W. Murphy (Sagamihara: ISAS), 159
Knight, C. A., et al. 1971, Science, 172, 52
Königl, A. 1981, ApJ, 243, 700

Krichbaum, T. P., et al. 1997, A&A, 323, L17
Lähteenmäki, A., Valtaoja, E., & Wiik, K. 1999, ApJ, 511, 112
Lähteenmäki, A., & Valtaoja, E. 1999, ApJ, 521, 493
Lawson, A. J., McHardy, I. M., & Marscher, A. P. 1999, MNRAS, 306, 247
Leppänen, K. J., Zensus, J. A., & Diamond, P. J. 1995, AJ, 110, 2479
Lister, M. L. 1998, Ph.D. thesis, Boston Univ.
Lister, M. L., Marscher, A. P., & Gear, W. K. 1998, ApJ, 504, 702
Lister, M. L., & Smith, P. S. 2000, ApJ, 541, 66
Lovell, J. E. J. 2000, in Astrophysical Phenomena Revealed by Space VLBI, ed. H. Hirabayashi, P. G. Edwards, & D. W. Murphy (Sagamihara: ISAS), 301
Lovell, J. E. J., et al. 2000, in Astrophysical Phenomena Revealed by Space VLBI, ed. H. Hirabayashi, P. G. Edwards, & D. W. Murphy (Sagamihara: ISAS), 183
Maraschi, L., Ghisellini, G., & Celotti, A. 1992, ApJ, 397, L5
Maraschi, L., et al. 1994, ApJ, 435, L91
Marchenko, S. G., et al. 1999, BAAS, 194, 5028
Marchenko-Jorstad, S. G., Marscher, A. P., Mattox, J. R., Hallum, J., Wehrle, A. E., & Bloom, S. D. 2000, in Astrophysical Phenomena Revealed by Space VLBI, ed. H. Hirabayashi, P. G. Edwards, & D. W. Murphy (Sagamihara: ISAS), 305
Marscher, A. P., et al. 1999, BAAS, 195, 8902
Marscher, A. P., Marchenko-Jorstad, S. G., Mattox, J. R., Wehrle, A. E., & Aller, M. F. 2000, in Astrophysical Phenomena Revealed by Space VLBI, ed. H. Hirabayashi, P. G. Edwards, & D. W. Murphy (Sagamihara: ISAS), 39
Pearson, T. J. 1995, in Very Long Baseline Interferometry and the VLBA, ed. J. A. Zensus, P. J. Diamond, & P. J. Napier (San Francisco: ASP), 267
Pilbratt, G., Booth, R. S., & Porcas, R. W. 1987, A&A, 173, 12
Piner, B. G., Edwards, P. G., Wehrle, A. E., Hirabayashi, H., Lovell, J. E. J., & Unwin, S. C. 2000, ApJ, 537, 91
Preston, R. A., et al. 2000, in Astrophysical Phenomena Revealed by Space VLBI, ed. H. Hirabayashi, P. G. Edwards, & D. W. Murphy (Sagamihara: ISAS), 199
Rantakyrö, F. T., et al. 1998, A&AS, 131, 451
Readhead, A. C. S. 1994, ApJ, 426, 51
Reid, M. J., & Moran, J. M. 1988, in Galactic and Extragalactic Radio Astronomy, ed. G. L. Verschuur & K. I. Kellermann (New York: Springer), 255
Shen, Z. Q., et al. 1999, PASJ, 51, 513

Shepherd, M. C., Pearson, T. J., & Taylor, G. B. 1994, BAAS, 26, 987
Sikora, M., Begelman, M. C., & Rees, M. J. 1994, ApJ, 421, 153
Sincell, M. W., & Krolik, J. H. 1994, ApJ, 430, 550
Slysh, V. I. 1992, ApJ, 391, 453
Steffen, W., Zensus, J. A., Krichbaum, T. P., Witzel, A., & Qian, S. J. 1995, A&A, 302, 335
Tateyama, C. E., Kingham, K. A., Kaufmann, P., Piner, B. G., de Lucena, A. M. P., & Botti, L. C. L. 1998, ApJ, 500, 810
Teräsranta, H., et al. 1992, A&AS, 94, 121
Teräsranta, H., et al. 1998, A&AS, 132, 305
Tornikoski, M., et al. 1996, A&AS, 116, 157
Unwin, S. C., Cohen, M. H., Biretta, J. A., Hodges, M. W., & Zensus, J. A. 1989, ApJ, 340, 117 (U89)
Unwin, S. C., Wehrle, A. E., Urry, C. M., Gilmore, D. M., Barton, E. J., Kjerulf, B. C., Zensus, J. A., & Rabaca, C. R. 1994, ApJ, 432, 103
Unwin, S. C., Wehrle, A. E., Xu, W., Zook, A. C., & Marscher, A. P. 1998, in Radio Emission from Galactic and Extragalactic Compact Sources, ed. J. A. Zensus, G. B. Taylor, & J. M. Wrobel (San Francisco: ASP), 69

Urry, C. M. 1999, Astropart. Phys., 11, 159
Valtaoja, E., Lähteenmäki, A., Teräsranta, H., & Lainela, M. 1999, ApJS, 120, 95
Wardle, J. F. C., Cawthorne, T. V., Roberts, D. H., & Brown, L. F. 1994, ApJ, 437, 122
Webb, J. R., Carini, M. T., Clements, S., Fajardo, S., Gombola, P. P., Leacock, R. J., Sadun, A. C., & Smith, A. G. 1990, AJ, 100, 1452
Wehrle, A. E. 1999, Astropart. Phys., 11, 169
Wehrle, A. E., Unwin, S. C., & Zook, A. C. 1994, in NRAO Workshop 23, Compact Extragalactic Radio Sources, ed. J. A. Zensus & K. I. Kellermann (Green Bank: NRAO), 197
Wehrle, A. E., Unwin, S. C., Zook, A. C., Urry, C. M., Marscher, A. P., & Teräsranta, H. 1996, in Blazar Continuum Variability, ed. H. R. Miller, J. R. Webb, & J. C. Noble (San Francisco: ASP), 430
Wehrle, A. E., et al. 1998, ApJ, 497, 178
Whitney, A. R., et al. 1971, Science, 173, 225
Zensus, J. A., Cohen, M. H., & Unwin, S. C. 1995, ApJ, 443, 35